Microwave-pumped semiconductor-superlattice parametric oscillator: a new subterahertz and terahertz radiation source

DISSERTATION

zur Erlangung des Doktorgrades der Naturwissenschaften (Dr. rer. nat.)

der Fakultät für Physik der Universität Regensburg

vorgelegt von

Benjamin Ingo Stahl

Juni 2008

Promotionsgesuch eingereicht am:	13.06.2008	
Die Arbeit wurde angeleitet von:	Prof. Dr. K. F. Renk	
Prüfungsausschuss:	Vorsitzender:	Prof. Dr. G. Bali
	1. Gutachter:	Prof. Dr. K. F. Renk
	2. Gutachter:	Prof. Dr. W. Wegscheider
	weiterer Prüfer:	Prof. Dr. J. Zweck

Contents

Abstract

The superlattice parametric oscillator (SPO), which was developed within the research for my doctoral thesis, is described. The research on the SPO comprised an experimental and a theoretical part. The SPO is pumped with microwave radiation and oscillates at the third harmonic frequency of the pump frequency. A semiconductor superlattice acts as active element giving rise to parametric gain for third harmonic radiation. A resonator delivers the feedback necessary for parametric oscillation. The SPO works at room temperature. We realized the SPO in a metal waveguide technique. When pumped with radiation of a frequency near 100 GHz it generated third harmonic radiation near 300 GHz. It was tunable over a broad frequency range. The SPO showed characteristic behavior of an oscillator. The power (0.1 mW) of the third harmonic radiation corresponded to a conversion efficiency of a few percent of the power (4 mW) of the pump radiation. Parametric gain is based on miniband electron transport in a superlattice. A theoretical analysis shows that gain can occur also at terahertz (THz) frequencies. Terahertz gain should allow it to realize a terahertz-SPO.

The SPO consisted of a double-waveguide structure with a quasiplanar superlattice device coupled by antennae to a third harmonic waveguide resonator and to a pump waveguide. Two reflectors terminated the resonator: one reflector was formed by a backshort, the other one, a partial reflector, occurred as a consequence of an impedance mismatch between the output port of the resonator waveguide and a horn antenna. Radiation was coupled out through the horn antenna. In a modified SPO design, the resonator length could be varied by a movable backshort.

For the quasiplanar SPO and for the modified SPO, different types of GaAs/AlAs superlattices were designed. The superlattice material was grown by molecular beam epitaxy. The superlattice devices were structured by means of photo lithography, metal vapor deposition, reactive ion etching and wet etching techniques.

The superlattice which was used in the quasiplanar SPO had 18 periods, each period

consisting of 14 monolayers GaAs and 4 monolayers AlAs, resulting in a miniband width of 25 meV. Superlattice devices were prepared in a quasiplanar design with a gold film bridge. For the modified SPO, superlattices with 60 periods (14 monolayers GaAs, 2 monolayers AlAs) and a miniband width of 140 meV were used. Superlattice devices with superlattice mesa structures (diameter 4 μm) were prepared.
The superlattice devices showed nonlinear, antisymmetric current-voltage characteristics. A characteristic indicated an ohmic behavior of the superlattice for low voltages and a peak current at a critical voltage. At higher voltages, the current decreased with increasing voltage, displaying a negative differential mobility. From the current voltage characteristics, the intraminiband electron relaxation time τ was estimated to be about 150 fs for both superlattices.
In various experiments, the quasiplanar SPO, as well as the modified SPO, showed properties which are characteristic for oscillators: feedback, threshold behavior, an influence of the resonator output coupling on the pump threshold , an optimum output coupling and an influence of an external resonator, coupled to the SPO, on the starting behavior. In the frequency range that was investigated, the SPO was continuously tunable from 225 GHz to 295 GHz.

The theoretical treatment of the SPO is based on a semiclassical single electron theory. Using the miniband electron dispersion relation and the acceleration theorem, a description of miniband electron transport under the influence of a time dependent electric field is derived. For a time dependent electric field consisting of a pump field and a third harmonic field, superlattice properties in the SPO (pump and third harmonic mobility and resistance, harmonic power, conversion efficiency) are determined, allowing to analyze the SPO mechanism.
The theoretical treatment shows that miniband transport in the SPO is strongly nonlinear. The nonlinearity gives rise to parametric gain for third harmonic radiation. The theory is in accordance with the experimental results. It explains the working principle of the SPO which produces radiation at subterahertz frequencies. If the pump power exceeds a certain threshold pump power, third harmonic gain occurs. Gain is present from zero amplitude of the third harmonic field on and increases with increasing amplitude, which enables the SPO to start oscillating by itself. The theoretical conversion

efficiency for our quasiplanar SPO is about 10 percent.
Beyond SPO operation at subterahertz frequencies, the theory shows that with an SPO, it is possible to efficiently generate radiation in the terahertz frequency range. At subterahertz frequencies, the condition $\omega\tau < 1$ is fulfilled, where ω is the oscillation frequency, whereas in the THz frequency range, $\omega\tau > 1$ is valid; $\omega\tau = 1$ corresponds to an oscillation frequency $\omega/2\pi$ of 1 THz. The threshold pump amplitude necessary to obtain parametric gain increases almost linearly with the oscillation frequency. With our superlattice material, oscillation frequencies of up to 10 THz should be achievable. The optimum operation conditions of a 3 THz SPO are determined. An SPO operating at 3 THz is predicted to have a conversion efficiency of up to 24 percent.

Further analyses of SPO operation at higher harmonics and of operation of a double-resonance SPO are presented. It is shown that in principle it is possible to realize an SPO working at the seventh or eleventh harmonic of the pump frequency. The theory also shows that at some harmonics (fifth, ninth, thirteenth), oscillations are not possible if only the pump and the harmonic field are taken into account. For these harmonics, parametric oscillations become possible if additionally a parametric oscillation at a lower harmonic is present (double resonance). The possibility to realize a double-resonance oscillator for the ninth harmonic is discussed.

The SPO is a room-temperature operated, broadband-tuneable subterahertz and terahertz radiation source. Regarding the high conversion efficiency in the THz frequency range, it might outperform other sources available today (e.g. Schottky multiplier chains). Through operation at higher harmonics, a superlattice parametric oscillator, pumped at moderate frequencies (e.g. 200 GHz), may be a practicable radiation source for the terahertz frequency range.

Abstract

1 Introduction

The terahertz (THz) frequency range from 1 THz to 10 THz, as well as the subterahertz frequency range from 0.1 THz to 1 THz, are of great interest not only for various fields of science but also for technological applications [1]. While for frequencies up to about 100 GHz (microwave radiation) and for the infrared range, compact, coherent, room-temperature operated solid state sources are available, there is a lack of such sources for frequencies from 0.1 THz to 10 THz. In a part of the literature, the 0.1 THz to 10 THz range is referred to as the terahertz range.

Especially in radio astronomy, the subterahertz and terahertz frequency range attracts much attention. Results from the NASA Cosmic Background Explorer (COBE) indicate that 98 percent of the photons emitted since the Big Bang fall into the subterahertz, terahertz and mid-infrared range [1]. Rotation and vibration lines of many molecules are found predominantly in the subterahertz and terahertz range as well as most of the emissions from interstellar dust [2]. For the detection of these lines, heterodyne receivers with local oscillators working at subterahertz and terahertz frequencies are necessary. At the end of 2008, ESA is planning to launch the space observatory Herschel, which is going to carry a heterodyne spectrometer for the subterahertz and terahertz frequency range, being able to detect radiation from 480 GHz to 1920 GHz [3]. Terahertz radiation can be used to study spectral properties of molecules [4] or for sensing of gas molecules or radicals (like OH) in the atmosphere. Terahertz imaging can be applied in material science, biology or medical diagnostics, where it is beneficial that the radiation is non-ionizing.

With respect to technical applications, the security sector seems to be most interested in this new technology. Terahertz imaging [5] is already used at airports and might be used at other public places like railway stations, metros or stadiums. As clothing is almost transparent for subterahertz radiation, concealed weapons can be detected with a subterahertz radar. Moreover, characteristic absorption spectra in the terahertz range

allow it to identify explosives or illicit drugs. However, the surveillance of public places with terahertz imaging, where persons appear more or less naked on a monitor, raises ethical questions [6]. Indoor communication systems using terahertz radiation will offer higher bandwidths than available on the microwave bands today. Such communication systems are tap-proof, as terahertz radiation is strongly damped by water vapor and by most construction materials used in buildings [7].

At present, various sources exist which deliver radiation in the subterahertz or terahertz frequency range but all of them have disadvantages for practical application.

A recent development towards a current-driven, solid state, monochromatic terahertz radiation source is the terahertz quantum cascade laser. Terahertz quantum cascade lasers with oscillation frequencies between 1.59 THz and 5 THz have been reported [8]. However, the realization of quantum cascade lasers at lower frequencies faces difficulties. One of them is that for the generation of a 1 THz photon, an intersubband separation of only 4 meV is required which is of the order of the intersubband level broadening. Terahertz quantum cascade lasers have to be cooled down to temperatures near liquid nitrogen temperature, often far below; frequency tuning can be obtained to a limited extent via temperature variation. Recently, a terahertz quantum cascade laser has been reported [9] which operated simultaneously at two frequencies ($\sim$ 34 THz and $\sim$ 39 THz) and produced terahertz radiation (frequency $\sim$ 5 THz, power $\sim$ 60 nW) by intracavity difference-frequency generation. The active region of the laser had a highly nonlinear susceptibility, leading to frequency mixing of the two signals. The laser was operated at room temperature. Further development of this technique may lead to a compact, room temperature radiation source at fixed frequencies within the whole terahertz range.

A further possibility to generate terahertz radiation is frequency downconversion from the optical or near-infrared regime. Optical parametric oscillators [10, 11] using a nonlinear optical crystal deliver pulsed terahertz radiation. Another technique is photomixing [1, 12], where two optical lasers are focused onto a photoconducting gap between two parts of an antenna to which a static voltage is applied. The lasers induce a photocurrent which is modulated with the difference-frequency between the frequencies of the two lasers. Photomixing delivers coherent radiation with powers of around 1 μW. Both methods, photomixing and optical parametric oscillations, require pump

lasers and complicated optical setups.

In the microwave regime, current-driven oscillators [13] using Gunn diodes, resonant tunneling diodes or IMPATT diodes deliver a power of the order of 100 mW at frequencies of about 100 GHz. But the power falls off steeply with increasing frequency. At frequencies around 400 GHz most of these sources deliver a power of less than 1 μW. By means of frequency multiplication, the radiation from an oscillator can be converted to radiation at harmonic frequencies. With frequency multipliers or chains of multipliers that use Schottky diodes as nonlinear elements, radiation at terahertz frequencies has been obtained (e.g., for a $2 \times 2 \times 3$-chain: 100 μW at 1 THz, efficiency 1 percent, operation temperature 120 K [1]).

This thesis presents a novel kind of subterahertz and terahertz radiation source which makes use of a microwave-pumped semiconductor superlattice as active element. In 1970, Esaki and Tsu made the proposition [14] to realize artificial crystals, namely superlattices, by growing alternating layers of two different semiconductor materials. The potential in the superlattice, with a large superlattice period compared to the atomic lattice period, leads to the formation of minibands for electrons. Esaki and Tsu predicted that miniband electron transport can lead to a negative differential mobility, making a superlattice suitable as a high-frequency nonlinear element. Due to the large superlattice period, Bloch oscillations of miniband electrons were expected to occur at relatively low electric fields. Semiconductor superlattices have been fabricated by molecular beam epitaxy and showed miniband transport and negative differential mobility [15]. Bloch oscillations have been observed by femtosecond optical techniques [16]. The coherent electromagnetic radiation emitted by Bloch oscillating electrons has been detected directly by four-wave mixing [17]. Ktitorov showed in a theoretical study [18] that a superlattice in a static electric field can have a negative high-frequency conductivity up to frequencies larger than the electron relaxation frequency in the superlattice, namely up to the Bloch frequency, leading to Bloch gain for terahertz radiation. The Bloch frequency can be chosen by the magnitude of the electric field in a superlattice and can reach several terahertz. Accordingly, a voltage-biased superlattice should be suitable as an active element of a terahertz Bloch oscillator [19]. Gain for terahertz radiation has been concluded from a static-voltage induced anomalous THz-

transmissivity of an array of superlattices [20]. An oscillator with a static-voltage biased superlattice is a candidate for a room temperature, tunable, coherent THz radiation source [19, 21, 13]

An obstacle for a static-voltage driven superlattice oscillator is the formation of space-charge inhomogeneities [22] which may hinder Bloch gain. Static-voltage driven superlattice oscillators that have been realized until now [23, 24, 13] generate radiation due to propagating space-charge domains. The formation of space-charge domains in a static-field biased superlattice may be suppressed by a strong terahertz field [19]. Domain suppression in a shunted two dimensional superlattice, prepared by cleaved edge overgrowth, has been demonstrated [25].

With a high frequency pump source and without a static voltage, semiconductor superlattices have been used as nonlinear elements in frequency multipliers reaching subterahertz [26] and terahertz [4] frequencies.

There is yet another possibility to realize a radiation source with a microwave-pumped semiconductor superlattice. Romanov [27] considered parametric generation of uneven harmonics in a superlattice under the condition of strong nonlinearity; Pavlovich [28] predicted the amplification of a weak high-frequency field in a superlattice submitted to a pump field. In 2004, Klappenberger and Renk proposed [29] a superlattice oscillator which is pumped by a high-frequency field rather than by a static electric field and which oscillates at odd harmonics of the pump frequency.

In this work, a realization of a microwave-pumped semiconductor superlattice oscillator is presented, namely the Superlattice Parametric Oscillator (SPO). The SPO oscillates at the third harmonic frequency ($\sim$ 300 GHz) of the pump frequency. The SPO is a new type of a room-temperature operated radiation source which delivers monochromatic, broadband frequency tunable subterahertz and possibly terahertz radiation. In this thesis, the theoretical and experimental development of the SPO is described. According to the theoretical analysis, the SPO is also suitable for operation at terahertz frequencies.

The results presented in this work would not have been possible without intense collaboration. We have discovered SPO action during experiments with a superlattice frequency multiplier. For our experiments, we have used two devices: a frequency mul-

tiplier which was built by Dr. D. Pavelev from the Ioffe Institute and an SPO which we developed in Regensburg and for which superlattice material was grown by molecular beam epitaxy by Dr. D. Schuh and Prof. Dr. W. Wegscheider. The waveguide structure for the SPO constructed in Regensburg was designed by my colleague A. Rogl and manufactured together with W. Wendt from the mechanical workshop. Our superlattices were structured together with our diploma students M. Muthmann and C. Reichl. The work was financially supported by the DFG through the Graduiertenkolleg 638 "Nonlinearity and nonequilibrium in condensed matter".

In the course of the research on the SPO, the following papers have been published:

Articles:

- *Subterahertz superlattice parametric oscillator*, K. F. Renk, B. I. Stahl, A. Rogl, T. Janzen, D. G. Pavel'ev, Yu. I. Koshurinov, V. Ustinov, and A. Zhukov, *Physical Review Letters*, vol. 95, no. 12, pp. 126801 1-4, 2005.

- *Terahertz superlattice parametric oscillator*, A. Rogl T. Janzen D. G. Pavelev Yu. I. Koschurinov V.Ustinov K. F. Renk, B. I. Stahl and A. Zhukov, cond-mat/0502284, 2005.

- *Semiconductor-superlattice frequency mixer for detection of submillimeter waves*, K. F. Renk, A. Rogl, B. I. Stahl, A. Meier, Yu. I. Koschurinov, D. G. Pavelev, V. Ustinov, A. Zhukov, N. Maleev, and A. Vasilyev, *Int. J. Infrared Millim. Waves*, vol. 27, pp. 373–380, 2006.

- *A theoretical study of operation conditions for a terahertz superlattice parametric oscillator*, B. I. Stahl, A. Rogl, and K. F. Renk, *Physics Letters A*, vol. 359, no. 5, pp. 512–515, 2006.

- *Semiconductor-superlattice parametric oscillator for generation of sub-terahertz and terahertz waves*, K. F. Renk, A. Rogl, and B. I. Stahl, *Journal of Luminescence*, vol. 125, pp. 252–258, 2007.

- *Semiconductor-superlattice parametric oscillator as a subterahertz and possible terahertz radiation source*, K. F. Renk, A. Rogl, B. I. Stahl, M. Muthmann,

H. Appel, M. Jain, A. Glukovskoy, D. Schuh, and W. Wegscheider, *Advances in OptoElectronics*, 2007, doi:10.1155/2007/54042.

- *Double-resonance semiconductor superlattice parametric oscillator for generation of subterahertz radiation*, A. Rogl, K. F. Renk, B. I. Stahl, C. Reichl, D. Schuh, and W. Wegscheider, *Int. J. Infrared Millim. Waves*, 2008, doi:10.1007/s10762-008-9392-3

Conferences:

- *Semiconductor superlattice frequency multiplier for the submillimeter wavelength range*, K. F. Renk, A. Rogl, B. I. Stahl, F. Lewen, B. Vowinkel, G. Winnewisser, Yu. I. Koshurinov, D. G. Pavelev, V. Ustinov, A. Zhukov, and N. Maleev, 29^{th} *International Conference on Infrared and Millimeter Waves*, Karlsruhe, 2004.

- *Superlattice frequency multiplier for generation of terahertz radiation*, B. I. Stahl, K. F. Renk, A. Rogl, T. Janzen, D. G. Pavelev, Yu. I. Koshurinov, V. Ustinov, and A. Zhukov, *ISSTT, International Symposium on Space Terahertz Technology*, Goetheburg, 2005.

- *Microwave-pumped semiconductor-superlattice oscillators*, B. I. Stahl, K. F. Renk, and A. Rogl, 5^{th} *Regensburg Workshop on Quantum Heterostructures and THz Electronics*, Regensburg, 2008.

2 Principle of the Superlattice Parametric Oscillator (SPO)

A superlattice parametric oscillator (fig. 2.1) is pumped with microwave radiation (pump frequency ω_1) and generates third harmonic radiation (frequency $\omega_3 = 3\omega_1$) by a parametric oscillation. A semiconductor superlattice serves as the active element of the SPO.

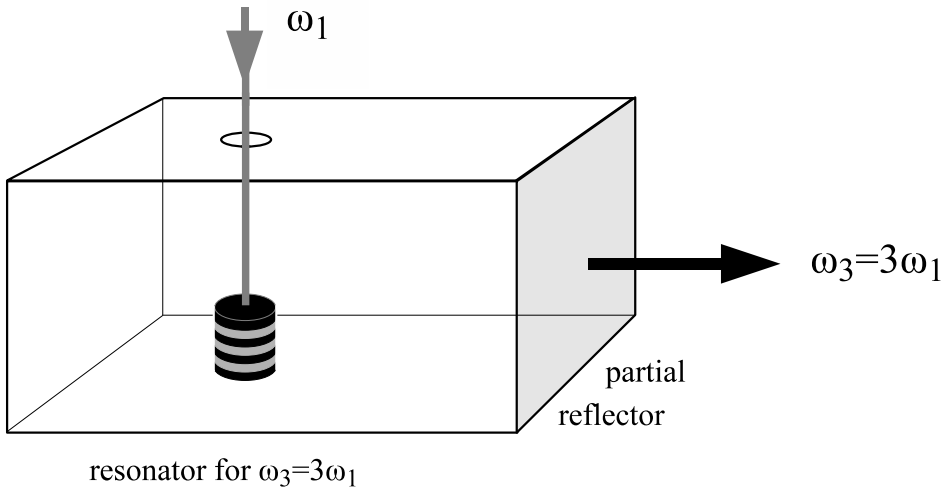

Figure 2.1: Principle of the superlattice parametric oscillator (SPO)

The semiconductor superlattice is coupled to a pump radiation source (frequency ω_1) and to a resonator for third harmonic radiation which delivers feedback for radiation at a frequency ω_3. The pump field brings the superlattice into an active state where it provides gain for third harmonic radiation. Through a partial reflector, radiation is coupled out from the resonator.

The SPO acts, effectively, as a frequency tripler. However, due to the feedback for third harmonic radiation and due to gain, the oscillation starts threshold-like. A much higher efficiency for conversion of pump radiation to third harmonic radiation is expected than for a conventional frequency tripler.

3 Theory

3.1 Electron transport in a semiconductor-superlattice

3.1.1 Superlattice structure and miniband formation

The semiconductor superlattices we used for our SPOs consisted of alternating layers of two different semiconductor materials, namely $GaAs$ and $AlAs$ (fig. 3.1). The layers were grown by molecular beam epitaxy, in (100) direction, onto a $GaAs$ substrate. A $GaAs$ layer and an adjacent $AlAs$ layer form one superlattice period (length a) along the superlattice axis x. The superlattice period length a (around 5 nm) is large compared to the period of the $GaAs$ lattice ($0,565$ nm). The superlattice axis x ((100) direction) is oriented perpendicularly to the superlattice layers.

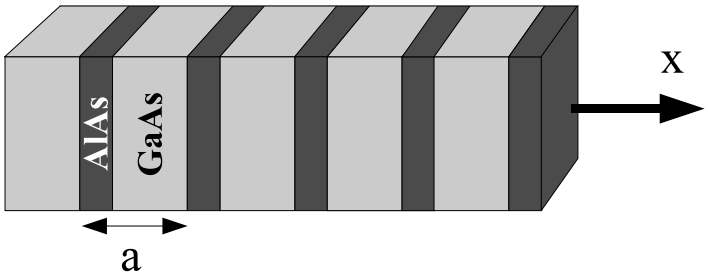

Figure 3.1: Schematic of a GaAs/AlAs-superlattice

For an electron moving along the superlattice axis, the $GaAs$ layers form potential wells (fig. 3.2), separated by AlAs barriers . Due to the periodicity of the superlattice potential, the electron energy for the motion in x direction is restricted to minibands. The lowest miniband (width Δ) is separated from the next higher miniband by a minigap.

The widths of the minibands and the minigaps in between them depend on the thickness of the wells and barriers (e.g. 18 monolayers of GaAs and 4 monolayers of AlAs result in a miniband width of 25 meV). Thus, the variation of the layer thicknesses allows to taylor the band structure of semiconductor superlattices. The band structure can be

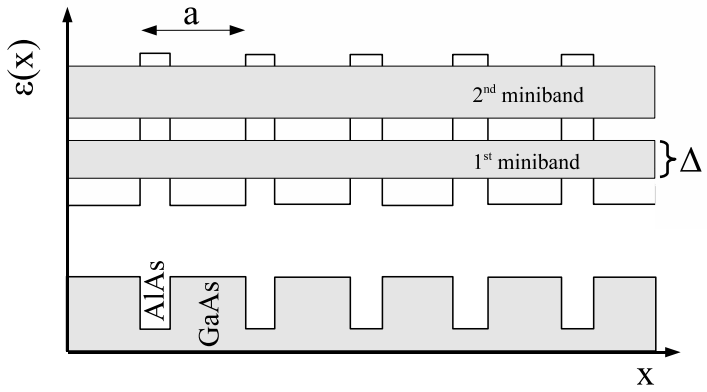

Figure 3.2: Band structure of a GaAs/AlAs-superlattice

calculated with the tight binding method [30].

Electron transport is carried by the lowest miniband. The energy dispersion relation for the lowest miniband (fig. 3.3) for motion along the superlattice axis x can be written as

$$\varepsilon(k) = \frac{\Delta}{2}(1 - \cos(ka)), \tag{3.1}$$

where $\varepsilon(k)$ is the electron energy and k the wave number along the superlattice axis x. The energy of the electron motion perpendicular to x is neglected.

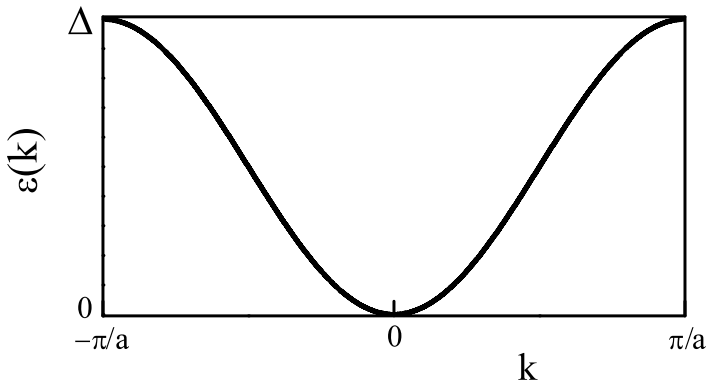

Figure 3.3: Dispersion relation for electron motion along the superlattice axis x.

3.1.2 Electron motion in a static electric field

Under the influence of an electric field parallel to the superlattice axis, an electron is accelerated according to the acceleration theorem

$$\hbar\dot{k} = eE(t), \tag{3.2}$$

where $E(t)$ is the time-dependent electric field strength and e the electron charge. The phase ka of the wave packet is

$$k(t, t_0)a = \int_{t_0}^{t} \frac{ea}{\hbar} E(t')dt', \tag{3.3}$$

where t_0 is the starting time of an electron with zero energy ($\varepsilon = 0$). The group velocity is obtained from the dispersion relation and is given by

$$v_g(t, t_0) = \frac{1}{\hbar}\frac{\partial\varepsilon(k)}{\partial k} = \frac{\Delta a}{2\hbar}\sin\left(k(t, t_0)\cdot a\right). \tag{3.4}$$

By substitution of $k(t, t_0)a$, using 3.3, the formula for v_g writes

$$v_g(t, t_0) = \frac{\Delta a}{2\hbar}\sin\left(\int_{t_0}^{t} \frac{ea}{\hbar} E(t')dt'\right). \tag{3.5}$$

This relation can be integrated and on obtains for the group velocity

$$v_g(t, t_0) = \frac{\Delta a}{2\hbar}\sin\left(\frac{ea}{\hbar}E_s\cdot(t - t_0)\right) = \frac{\Delta a}{2\hbar}\sin\left(\omega_B\cdot(t - t_0)\right). \tag{3.6}$$

In a static electric field E_s, the electron oscillates sinusoidally with the static-field dependent Bloch frequency

$$\omega_B = \frac{ea}{\hbar}E_s. \tag{3.7}$$

Bloch oscillation occurs due to Bragg reflection of an electron reaching the Brillouin zone boundary ($k = \frac{\pi}{a}$). Here, the electron energy reaches the upper miniband edge Δ. The periodic electron motion on a trajectory ξ is given by

$$\xi(t) = \frac{\Delta a}{\hbar\omega_B}\left(1 - \cos(\omega_B(t - t_0))\right) = \xi_0\left(1 - \cos(\omega_B(t - t_0))\right), \tag{3.8}$$

where $\frac{\Delta a}{\hbar\omega_B}$ is the spatial extension of the trajectory. When the electric field strength is large, so that $\hbar\omega_B = \Delta$, then $\xi_0 = a$ and the motion of the Bloch oscillating electron is limited to a single superlattice period. For such high fields, the miniband model is not valid any more.

Up to this point, electron motion without relaxation has been considered. Yet, in order to obtain electron transport, one has to take into account the effect of intraminiband

electron relaxation. An electron relaxation time τ, which is an average of the momentum and the energy relaxation time, is used. The electron drift velocity $v(t)$ can then be written as

$$v(t) = \frac{2v_p}{\tau} \int_{-\infty}^{t} p(t, t_0) \cdot v_g(t, t_0) dt_0, \tag{3.9}$$

where

$$p(t, t_0) = e^{-\frac{(t-t_0)}{\tau}} \tag{3.10}$$

is the probability that an electron does not undergo a relaxation process within the time interval $(t - t_0)$ and $v_p = \frac{\Delta a}{4\hbar}$ is the peak drift velocity at zero lattice temperature. The integration from $-\infty$ to t averages over all starting times of the electron. A theoretical treatment [31] using a one dimensional Boltzmann equation in relaxation time approximation, delivers the temperature-dependence of the peak drift velocity

$$v_{p,T} = \frac{\Delta a}{4\hbar} \frac{I_1(\frac{\Delta}{2k_B T})}{I_0(\frac{\Delta}{2k_B T})}, \tag{3.11}$$

where I_0, I_1 are the modified Bessel functions of zeroth and first order, T the lattice temperature and k_B the Boltzmann constant. The modified peak drift velocity takes into account the thermal equilibrium distribution function at finite temperature. At room temperature, the drift velocity is reduced by a factor of about 0.8, compared to zero temperature.

The integration of $v(t)$ leads to the Esaki-Tsu relation [14]

$$v = 2v_p \frac{\omega_B \tau}{1 + (\omega_B \tau)^2}. \tag{3.12}$$

By substitution of $\omega_B \tau$ the relation writes

$$v = 2v_p \frac{E_s/E_c}{1 + (E_s/E_c)^2}, \tag{3.13}$$

with $E_c = \frac{\hbar}{ea\tau}$ being the critical field strength of the superlattice. The function is depicted in figure 3.4. The curve shows a linear increase of the electron velocity at small field strengths and a maximum velocity v_p at the critical field strength $E = E_c$. At field strengths exceeding E_c, the electron velocity decreases with increasing field strength, leading to a negative differential mobility. The critical field strength corresponds to the condition $\omega_B \tau = 1$. This condition $\omega_B \tau = 1$ is fulfilled when the electrons reach the k value $\frac{\pi}{2a}$. Here, the dispersion relation has its inflection point. The effective mass

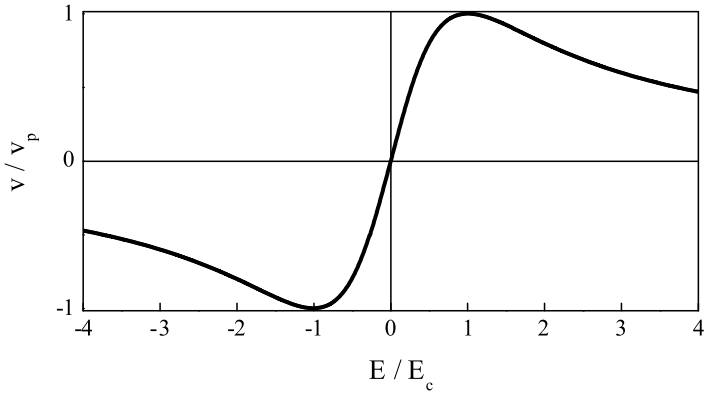

Figure 3.4: Esaki-Tsu current-voltage characteristic

changes from positive to negative values. In contrast to that, Bragg reflections ($k = \frac{\pi}{a}$) occur at field strengths where $\omega_B \tau \geq 2\pi$.

3.1.3 Electron motion in terahertz fields

The Esaki-Tsu characteristic is suitable to describe superlattice electron dynamics in a high frequency field (frequency ω for the condition that $\omega\tau << 1$. Then, the change of the electric field strength is slow enough in comparison to the electron relaxation time, so that the drift velocity $v(t)$ can follow the Esaki-Tsu curve. In order to characterize the electron dynamics in a high frequency field for all frequencies, the time-dependent electron drift velocity is directly calculated according to formula 3.9, leading to:

$$v(t) = \frac{2v_p}{\tau} \int_{-\infty}^{t} e^{-\frac{(t-t_0)}{\tau}} \sin\left(\int_{t_0}^{t} \omega_B(t')dt'\right) dt_0, \tag{3.14}$$

where

$$\omega_B = \frac{ea}{\hbar}(\hat{E}\cos\omega t) \tag{3.15}$$

is the dynamic Bloch frequency. The Bloch frequency is modulated by a high frequency field that is applied to the superlattice. The maximum of the dynamic Bloch frequency ($\omega_{B,max} = \frac{ea}{\hbar}(\hat{E})$) depends on the amplitude $\hat{E}$ of the pump field. For a pump amplitude $\hat{E} = 5E_c$, $\omega_{B,max}/2\pi$ is about 5 THz.

The results obtained by the direct calculation of the drift velocity $v(t)$ in a superlattice driven by a high frequency field $E(t) = \hat{E}\cos(\omega t)$ coincide with the results obtained from the Esaki-Tsu characteristic, only if the frequency ω is low enough. Figure 3.5 shows the time dependent drift velocity for pump frequencies from 10 GHz to 3 THz.

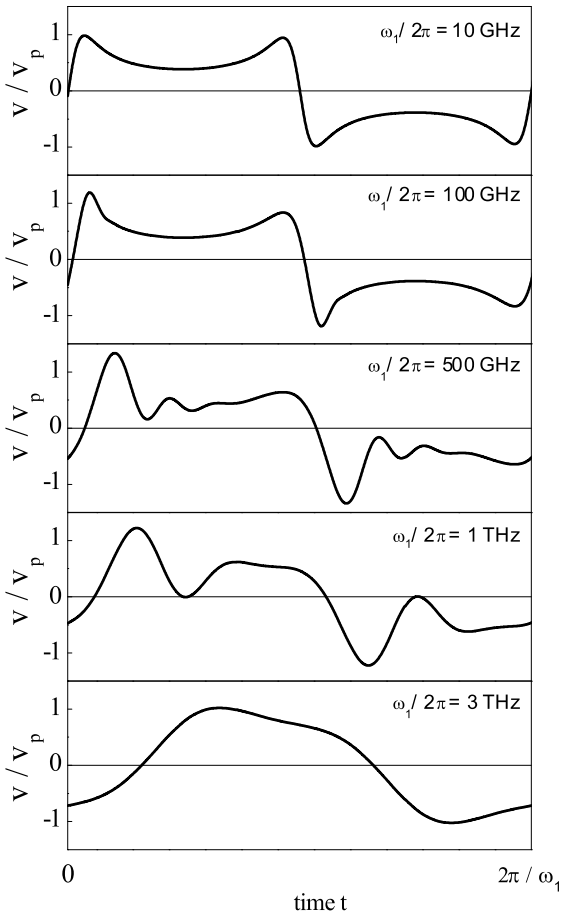

Figure 3.5: Electron drift velocity in a superlattice with a high frequency electric field. The electron drift velocity is depicted during one pump cycle for different pump frequencies ω_1.

For a frequency $\omega_1 = 2\pi \cdot 10$ GHz, the curve shows a steep increase, a peak ($v = v_p$), a decrease to a minimum ($v \sim 0.5 v_p$), an increase to a second peak ($v = v_p$) and thereafter a steep decrease to zero velocity. The curve is antisymmetric with respect to the zero crossing, showing a similar shape for negative velocities. At this pump frequency, the curve is in perfect agreement to what is obtained if a slowly changing DC field is applied to an ideal Esaki-Tsu superlattice. The velocity peaks are in agreement with the Esaki-Tsu characteristic. The minima in between the peaks correspond to the range of negative differential mobility. At a frequency of 100 GHz, which corresponds to $\omega_1 \tau \sim 0.1$, overshoot effects occur, where v reaches about 1.1 v_p. The second peak for each direction of the velocity is smaller than v_p. Concerning the frequency, this case is quite similar to our experimental situation. At higher frequency (500 GHz, $\omega_1 \tau \sim 0.5$), Bloch oscillations become directly visible in the drift velocity. At such

high frequency, the switching of the direction of the electric field happens very fast. The electron can perform a Bloch oscillation before relaxation takes place after the time τ. At a pump frequency $\omega_1 = 2\pi \cdot 1$ THz, the limit $\omega_1\tau = 1$ is reached, where the pump frequency is equal to the relaxation frequency $\frac{1}{\tau}$. The more ω_1 approaches the dynamic Bloch frequency, the more the Bloch oscillating electron directly follows the electric force (with a phase delay). Electron relaxation begins to play a subordinate role.

3.2 Theory of the SPO

3.2.1 Origin of gain

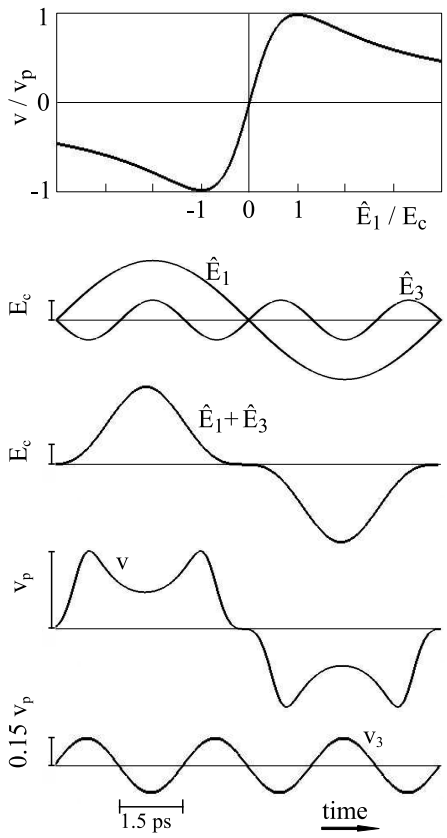

Figure 3.6: Illustration of the origin of gain in the superlattice parametric oscillator (SPO)

For an illustration of how gain occurs in an SPO, it is supposed that the electric-field dependent electron drift velocity follows the Esaki-Tsu characteristic (fig. 3.6 a). A pump field $E_1(t) = \hat{E}_1 \cos(\omega_1 t)$ with an amplitude that is larger than the critical field strength E_c switches the superlattice periodically into the active state. A third har-

monic field $E_3(t) = \hat{E}_3 \cos(\omega_3 t)$, which acts on the superlattice due to the feedback from the resonator, is superimposed to the pump field (fig. 3.6 b). The total field $E(t) = \hat{E}_1 \cos(\omega_1 t) + \hat{E}_3 \cos(\omega_3 t)$ causes an electron drift velocity $v(t)$. The third harmonic Fourier component of the drift velocity, $v_3(t) = \hat{v}_3 \cos(\omega_3 t)$, is of opposite phase compared to the electric field $E_3(t)$, as $\hat{v}_3$ is negative. Thus, the time average $\langle v_3 E_3 \rangle$, which is a measure for the third harmonic power, is negative. The third harmonic field is amplified, energy is transferred parametrically from the pump field to the third harmonic field. The pump amplitude $\hat{E}_1$ is chosen to be $3\hat{E}_3$. In this case, the total electric field stays zero for a maximal time and switches the superlattice fast (in comparison to a purely sinusoidal field) from a normal state with almost no absorption, through an absorptive state (ohmic region of the superlattice) to the active state, where negative differential mobility prevails. With the chosen ratio between pump and third harmonic field, losses are minimized and a maximal efficiency is expected.
For pump amplitudes below E_c, there is almost no gain, but miniband transport is already nonlinear. The superlattice produces third harmonic radiation without gain and feedback by ordinary frequency multiplication according to the nonlinear current-voltage characteristic. However, the conversion efficiency is very low.

3.2.2 Calculation of dynamic superlattice properties

The Esaki-Tsu model was used for an illustration of how gain occurs in the SPO. For an analysis of the SPO, a more general theory is used. The electron drift velocity

$$v(t) = \frac{2v_p}{\tau} \int_{-\infty}^{t} e^{-\frac{(t-t_0)}{\tau}} \sin\left(\frac{ea}{\hbar} \int_{t_0}^{t} E(t')dt'\right) dt_0, \tag{3.16}$$

is calculated for a time-dependent electric field $E(t) = \hat{E}_1 \cos(\omega_1 t) + \hat{E}_3 \cos(\omega_3 t)$ along the superlattice axis consisting of a pump field and a third harmonic field.
Having calculated the drift velocity $v(t)$ for one period of the pump field $E_1(t)$, the Fourier components $v_i = \hat{v}_i \cos(\omega_i t)$ for different harmonics of the pump frequency are determined by means of a fast Fourier Transformation (FFT) (fig. 3.7).
For the drift velocity depicted in figure 3.5, 100 GHz, a positive Fourier component v_1 is obtained at the pump frequency. The third harmonic v_3, the seventh harmonic v_7 and the eleventh harmonic v_{11} are negative, while v_5, v_9 and v_{13} are positive. The Fourier coefficients $\hat{v}_i$ are positive for $i = 1 + 4m$ and negative for $i = 3 + 4m$ $(m = 0, 1, 2...)$.

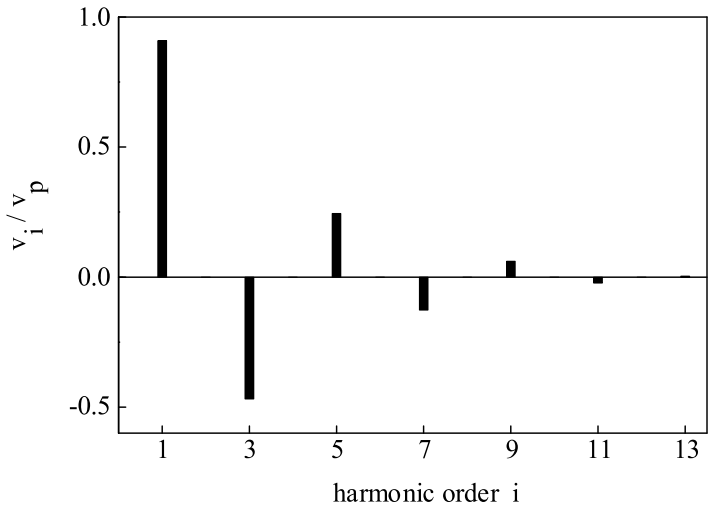

Figure 3.7: Electron drift velocity components for different harmonic frequencies of the pump frequency

Even harmonics do not occur due to the symmetry of the superlattice, and to the antisymmetry of the current-voltage characteristic, respectively.

From the amplitudes $\hat{v}_i$, one obtains the corresponding current amplitudes $\hat{I}_i$ with the relation

$$\frac{\hat{I}_i}{I_p} = \frac{\hat{v}_i}{v_p}, \tag{3.17}$$

with the peak current $I_p = neAv_p$, where n is the conduction electron density and A the cross-sectional area of the superlattice. The voltage amplitudes $\hat{U}_i$ across the superlattice and the critical voltage U_c are calculated using

$$\frac{\hat{U}_i}{U_c} = \frac{\hat{E}_i}{E_c}. \tag{3.18}$$

The high frequency mobilities μ_i are defined by

$$\mu_i = \frac{\hat{v}_i}{\hat{E}_i} \tag{3.19}$$

At small electric fields, an Esaki-Tsu superlattice has the ohmic mobility $\mu_0 = \frac{2v_p}{E_c}$.

The high frequency resistances R_i for the different harmonics are obtained according to

$$R_i = \frac{\hat{U}_i}{\hat{I}_i}. \tag{3.20}$$

The ohmic resistance R_0 of a superlattice is given by $R_0 = \frac{U_c}{2I_p}$; the harmonic power P_i is calculated according to $P_i = \frac{1}{2}\hat{U}_i\hat{I}_i$. If P_i is negative, radiation energy (frequency $\nu_i = 2\pi\omega_i$) is transferred from the superlattice to the radiation field in the resonator. The efficiency η_{ij} for conversion of radiation from the j^{th} to the i^{th} harmonic frequency is obtained from

$$\eta_{ij} = \left|\frac{P_i}{P_j}\right|. \tag{3.21}$$

The drift velocities, resistances, powers and efficiencies for different pump and harmonic ratios as well as frequencies are used to characterize the superlattice dynamics in the SPO. By relating the results to basic superlattice properties like the peak power $P_p = U_c \cdot I_p$, the ohmic resistance R_0 or the ohmic mobility μ_0 , they can be discussed independently of the superlattice type. In the further discussion, voltage amplitudes $\hat{U}$ will be used instead of electric field amplitudes $\hat{E}$, since a discussion of voltages is more understandable with respect to the experiments.

3.3 Theoretical results

3.3.1 Parametric gain

For a theoretical analysis of the SPO, parameters are chosen which fit the conditions in the experiments shown later. From the experimental data, it can be estimated that the pump voltage amplitude at the superlattice is about $3\,U_c$; the pump frequency of about 100 GHz corresponds to $\omega_1\tau \sim 0.1$. The dependence of the third harmonic mobility μ_3 on the pump voltage amplitude $\hat{U}_1$ is calculated (fig. 3.8) for three different third harmonic amplitudes $\hat{U}_3$ ($0.5\,U_c, 1.0\,U_c$ and $1.5\,U_c$).

The mobility μ_3 is positive for zero pump amplitude $\hat{U}_1$. With increasing $\hat{U}_1$, the mobility decreases until it becomes negative. The pump amplitude where μ_3 becomes negative depends on the third harmonic amplitude $\hat{U}_3$. The larger the third harmonic amplitude, the higher is the pump amplitude necessary to obtain a negative mobility. A negative third harmonic mobility for a certain pump amplitude $\hat{U}_1$ and third harmonic amplitude $\hat{U}_3$ indicates that under these conditions, the superlattice provides gain for third harmonic radiation.

A pump voltage amplitude $\hat{U}_1 = 3\,U_c$ is sufficient for gain, if $\hat{U}_3$ is smaller than $1.5\,U_c$.

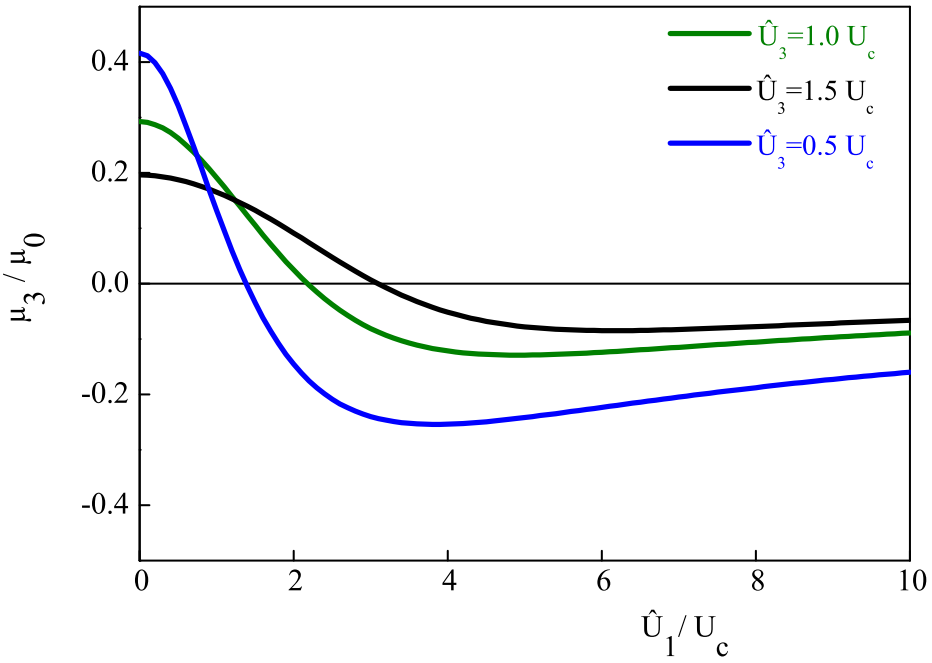

Figure 3.8: Dependence of the third harmonic mobility on the pump amplitude for three different third harmonic amplitudes. A negative mobility indicates parametric gain for third harmonic radiation.

3.3.2 Optimum operation conditions of a subterahertz SPO

The properties of a superlattice in an SPO, which is pumped with an amplitude $\hat{U}_1 = 3\,U_c$ are investigated. The third harmonic mobility μ_3, resistance R_3, power P_3 and conversion efficiency η_3 and the pump resistance R_1 are calculated for different values of the third harmonic amplitude $\hat{U}_3$ (fig 3.9). The mobility μ_3 (fig. 3.9a) is negative at $\hat{U}_3 = 0$. With increasing $\hat{U}_3$ the absolute value of the mobility decreases until it switches to positive values at $\hat{U}_1 \sim 1.5\,U_c$. The corresponding resistance R_3 (fig. 3.9b) is negative for small $\hat{U}_3$. The absolute value increases and has a singularity corresponding to the zero-point of μ_3, where R_3 becomes positive. The third harmonic power P_3 (fig 3.9c) is negative between $\hat{U}_3 = 0$ and $\hat{U}_3 = 1.5\,U_c$. In-between, there is an extreme value where P_3 reaches almost $-0.32\,P_p$. This optimum is located close to $\hat{U}_3 = 1\,U_c$. The corresponding maximum of the conversion efficiency η_{31} (fig. 3.9d) is thirteen percent. Within the range of $\hat{U}_3$ where gain occurs, the pump resistance R_1 (fig. 3.9e) is almost constant. The parameters where the efficiency is maximal define the optimum operation conditions. The optimum operation conditions vary with the frequency and the pump amplitude.

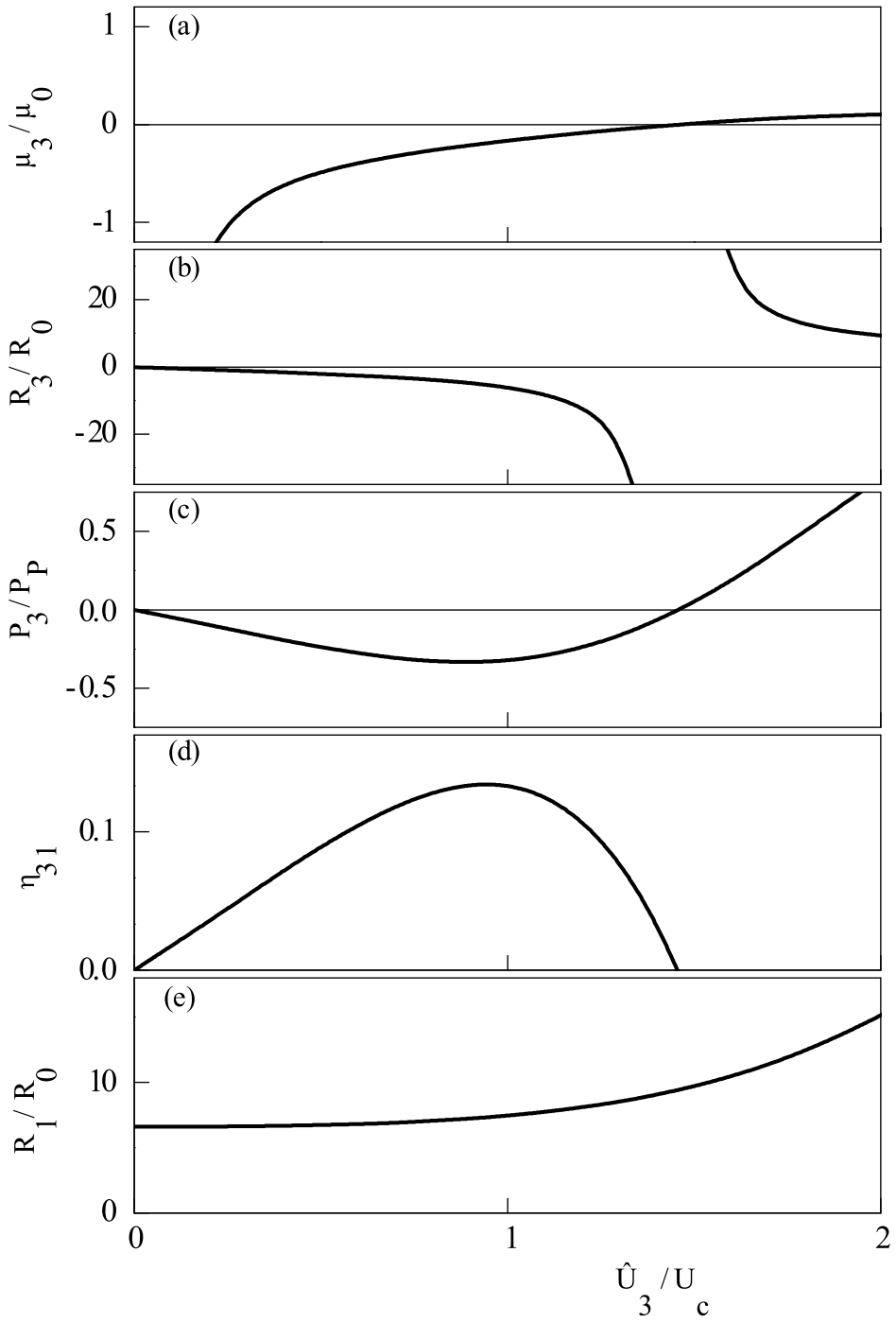

Figure 3.9: Dependence of the third harmonic mobility (a), resistance (b), power (c) and conversion efficiency (d) and of the pump resistance (e) on the third harmonic amplitude $\hat{U}_3$.

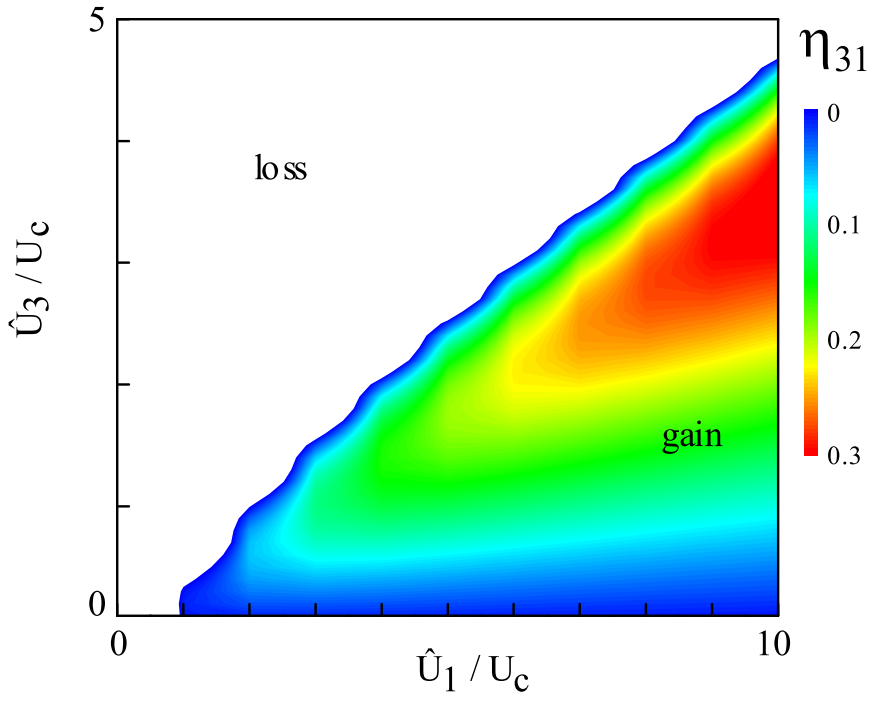

Figure 3.10: Efficiency of an SPO, operated at 300 GHz, for different values of the pump and third harmonic amplitudes.

In order to gain an overview over the operation conditions of the SPO the conversion efficiency η_{31} for different pump and third harmonic amplitudes (fig 3.10) has been calculated. The efficiency reaches up to 30 percent if the pump amplitude is increased to about $10\,U_c$. The corresponding third harmonic amplitude has to be around $3\,U_c$. For a pump frequency of 100 GHz, one can roughly state that the superlattice mobility becomes positive if $\hat{U}_3 \geq \frac{\hat{U}_1}{2}$ and that the optimum third harmonic amplitude is about one third of the pump amplitude.

Phase conditions

Our discussion did not include a phase between the pump and third harmonic field applied to the superlattice. For the calculations, a total voltage $U(t) = \hat{U}_1 \cos(\omega_1 t) + \hat{U}_3 \cos(\omega_3 t + \phi)$ was used, with the phase ϕ of the third harmonic voltage being zero. This situation is consistent with our intuitive illustration of gain in an SPO.

For the optimum operation conditions determined before, the third harmonic power was calculated for different phases ϕ between 0 and 2π (fig. 3.11). The absolute value of the power is maximal for zero phase ($\sim 0.5 P_p$). At a phase $\phi = \pi$, the power is

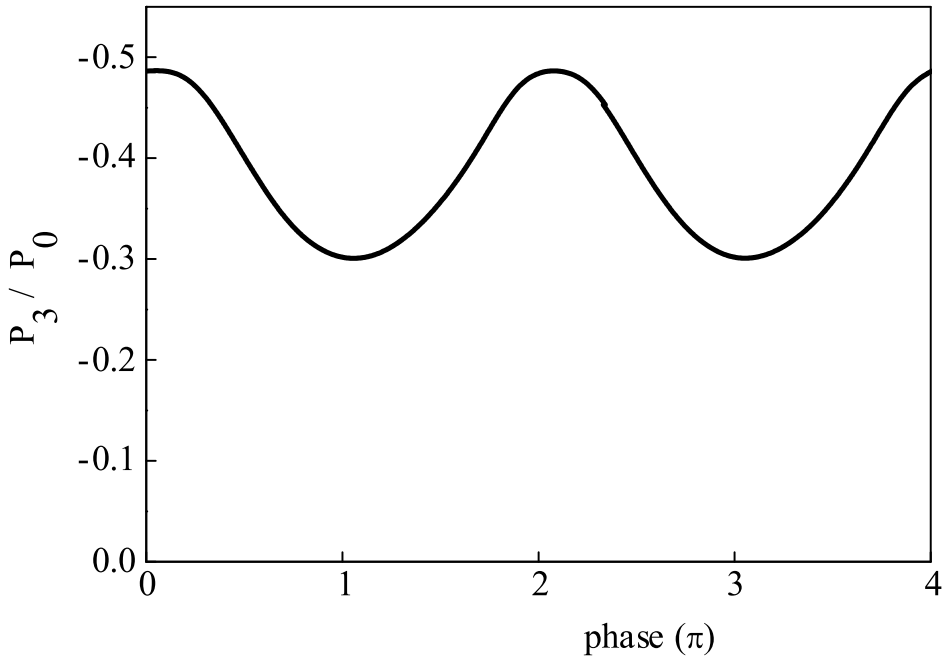

Figure 3.11: Dependence of the power P_3 of an SPO on the phase ϕ of the third harmonic field

reduced by about 40 percent.

Oscillation onset and adaption to resonator circuit

In our SPO, a pump voltage $U_1 = \hat{U}_1 \cos(\omega_1 t)$ is applied to the superlattice which is coupled to a third harmonic resonator. Due to the nonlinear transport properties of the superlattice, a small amount of third harmonic radiation is produced by frequency multiplication and emitted to the resonator. The third harmonic field in the resonator again causes a voltage $U_3 = \hat{U}_3 \cos(\omega_3 t)$ at the superlattice. Due to the negative mobility, the signal is amplified and an oscillation starts to build up.

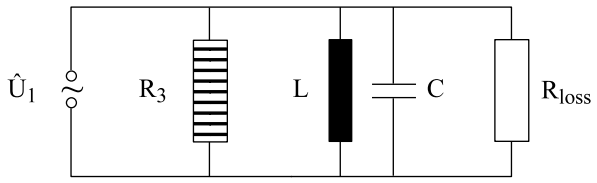

Figure 3.12: Equivalent circuit for an SPO. The resistance R_{loss} represents the resonator losses. In the steady state, the third harmonic power generated by the superlattice (represented by R_3) has to be completely coupled out from the resonator, requiring that $R_3 = -R_{loss}$.

We found that the mobility μ_3 is negative from $\hat{U}_3 = 0$ on, which in principle enables

the oscillator to start from noise. Actually, a pumped superlattice always produces a small amount of third harmonic radiation due to frequency multiplication. A third harmonic field builds up in the resonator to which the superlattice is coupled. When the third harmonic amplitude $\hat{U}_3$ increases during the start of the oscillation, also $|R_3|$ increases (see fig. 3.9).

If we describe the SPO by means of an equivalent circuit (fig. 3.12), the resonator for the third harmonic is formed by an inductance, a capacitance and a resistance R_{loss} which represents the losses from the resonator, which are primarily caused by the output coupling. In the steady state, the third harmonic power that is generated has to be completely coupled out of the resonator, i.e., P_3 has to be completely consumed by R_{loss}, which can be expressed by the condition $-P_3 \stackrel{!}{=} P_{loss}$. It follows that $\frac{1}{2}\hat{U}_3^2/R_3 = -\frac{1}{2}\hat{U}_3^2/R_{loss}$, assuming that the third harmonic voltage amplitude is the same for all components of the circuit. Accordingly, one obtains the condition that

$$R_3 = -R_{loss}. \tag{3.22}$$

In the real SPO the relevant resistance will be the one the resonator provides to the superlattice. The third harmonic field in an SPO automatically adjusts to a strength where equ. 3.22 is fulfilled. By adjusting R_{loss} via the output coupling of the resonator, it is possible to choose the third harmonic amplitude for maximal P_3.

4 Experimental realization

4.1 SPO realization

4.1.1 Quasiplanar SPO design

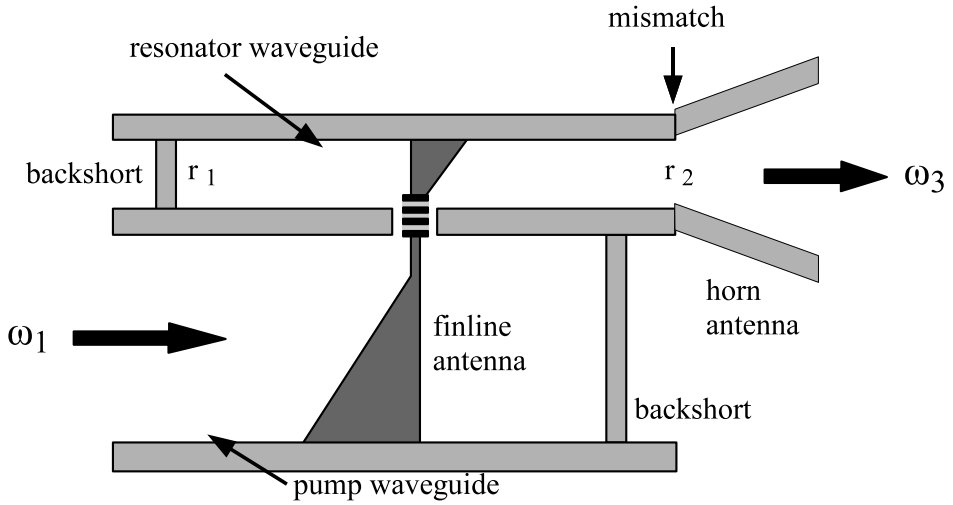

Figure 4.1: Schematic of the quasiplanar SPO, realized in waveguide technique.

The SPO (fig. 4.1) was realized in a double-waveguide structure. Two rectangular waveguides, a pump waveguide (2.54 mm wide and 1.27 mm high) and a waveguide that served as resonator (0.8 mm wide and 0.4 mm high) were milled into a cuboid block of brass. The two parallel waveguides were separated by a thin wall. The wall had a feedthrough where the superlattice device was located. The superlattice device had two gold film terminals for connection, one on each side. One gold film contact was connected, with a conductive glue, to a finline antenna. The antenna was located in the pump waveguide in order to couple the superlattice to the pump field. The gold film contact on the other side of the superlattice was connected to a finline antenna in the resonator waveguide, coupling the superlattice to the third harmonic field. The third harmonic resonator was terminated by two reflectors, on one side a reflector was formed by a backshort, on the other side, an impedance mismatch between the

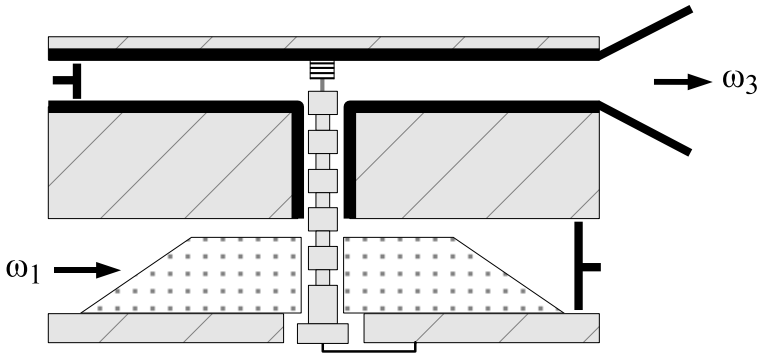

Figure 4.2: Schematic of the modified SPO with adjustable resonator length.

waveguide output port and a horn antenna served as a partial reflector. The length of the resonator was about 10 mm. Radiation was emitted from the horn antenna having a narrow lobe-shaped radiation pattern.

4.1.2 Modified SPO design with variable resonator length

A second SPO in a modified design was constructed. By means of a movable backshort, the resonator length was variable. The SPO (fig. 4.2) consisted of a double-waveguide structure. It contained a pump waveguide (2.54 mm wide and 1.27 mm high), a resonator waveguide (0.8 mm wide and 0.4 mm high) and a coaxial structure (length 1.5 mm), which connected the pump and the resonator waveguide. The superlattice was mounted in the resonator waveguide. The pump field and the third harmonic field were coupled to the superlattice by a whisker antenna that was fixed to the coaxial structure. The coupling between the coaxial structure and the pump waveguide was achieved by a fin line antenna. By means of a movable backshort, the length of the pump waveguide could be adjusted for optimal input coupling. The coaxial structure was designed as a band stop filter for the third harmonic, preventing loss of third harmonic radiation to the pump waveguide. It could either be connected to ground during SPO operation or to a voltage source for measuring the current-voltage characteristic of the superlattice. A movable backshort in the resonator was used to vary the resonator length. The mismatch between resonator waveguide and a horn antenna was a partial reflector through which radiation was coupled out.

4.2 Superlattice structures

4.2.1 Quasiplanar superlattice device

The superlattice material was grown by molecular beam epitaxy (MBE) onto a semi-insulating $GaAs$ substrate. It consisted of the $GaAs$ substrate, an n^+ $GaAs$ layer (1.5 μm thick, Si-doping level $6 \cdot 10^{18}$ cm^{-3}), a gradual layer (32 nm thick), the superlattice itself, another gradual layer, an n^+ $InGaAs$ gradual layer (25 nm) and, finally an n^+ $InGaAs$ layer (20 nm, 10^{19} cm^{-3}). The gradual layers delivered a smooth transition of doping levels and layer thicknesses. The superlattice (length $L = 112$ nm) had 18 periods (period length $a = 6.23$ nm), each of them consisted of 18 monolayers $GaAs$ and 4 monolayers $AlAs$ with a homogeneous Si-doping level of $1 \cdot 10^{18}$ cm^{-3}. The miniband width of the superlattice was about 25 meV

The superlattice device (fig. 4.3, left) was structured in a quasi planar design by photo lithography. It was 200 μm long, 150 μm wide and 20 μm thick. The connection from one contact film, which was on the top of a supporting superlattice to the active superlattice (diameter $\sim$ 1.5 μm) was provided via a gold film bridge. The gold film bridge, which was obtained by an underetching process, was 10 μm long and 1 μm wide. The contact film on the other side was connected to the bottom of the active superlattice through a low-resistance, large-area superlattice and the n^+GaAs layer.

Different superlattice devices showed similar current-voltage curves. One is shown in figure 4.3. The superlattice device had an ohmic resistance $R_0 \sim 10\ \Omega$ near zero voltage and a negative differential resistance at voltages higher than a critical voltage, where the peak current $I_p \sim 7$ mA was reached. Taking into account an additional series resistance of 10 Ω, the IV curve was in agreement with the Esaki-Tsu characteristic for voltages smaller than the critical voltage $U_c \sim 0.2$ V. At higher voltage, the curve deviated from the Esaki-Tsu curve. This is most probably due to the formation of space charge domains [32]. The critical voltage U_c corresponded to a critical field strength $E_c = U_c/L = 10$ kV/cm, the peak current density j_p was about 200 kA/cm^2.

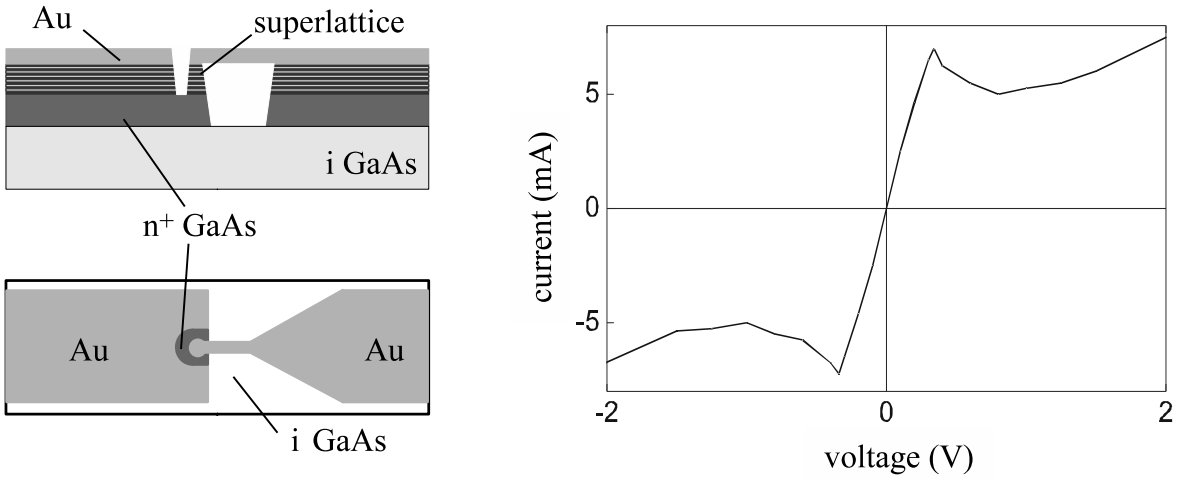

Figure 4.3: left: Schematic of the quasiplanar superlattice device used in the quasiplanar SPO. The GaAs/AlAs superlattice with 18 periods had a miniband width $\Delta = 25$ meV. right: DC current-voltage curve of the superlattice device measured outside the resonator

4.2.2 Superlattice device with mesas for the modified SPO

For the modified SPO, a different superlattice type was prepared having circular superlattice mesa structures (fig. 4.4 a).

The superlattice had 60 periods, each period (length $a = 4.52$ nm) consisted of 14 monolayers $GaAs$ and 2 monolayers $AlAs$. The superlattice was homogeneously doped with silicon (concentration $1 \cdot 10^{17}$ cm^{-3}) and had a large miniband width $\Delta \sim 140$ meV. The superlattice material was grown onto a semi-insulating $GaAs$ substrate by molecular beam epitaxy. The layer sequence consisted of a 1 μm thick n-doped $GaAs$ layer (concentration $2 \cdot 10^{18}$ cm^{-3}), a graded layer (18 nm thick), then the superlattice (length $L \sim 270$ nm), another graded layer and another n-doped $GaAs$ layer (200 nm thick). By use of photo lithography, metal vapor deposition and dry and wet etching processes, superlattice devices (fig. 4.4 a) were prepared. One device carried about 200 superlattice mesas of circular shape having a diameter of ~ 4 μm. Each mesa (fig. 4.4 b, inset) had an ohmic contact ($Ni/Ge/Au$-alloy) on top of it. Being used as an active element, a single mesa could be contacted from the top by an electro-chemically sharpened whisker antenna (diameter 25 μm). From the bottom, the superlattice was contacted via the n-doped $GaAs$ layer and a large-area superlattice.

The current-voltage characteristic (fig. 4.4, right) of the superlattice device showed

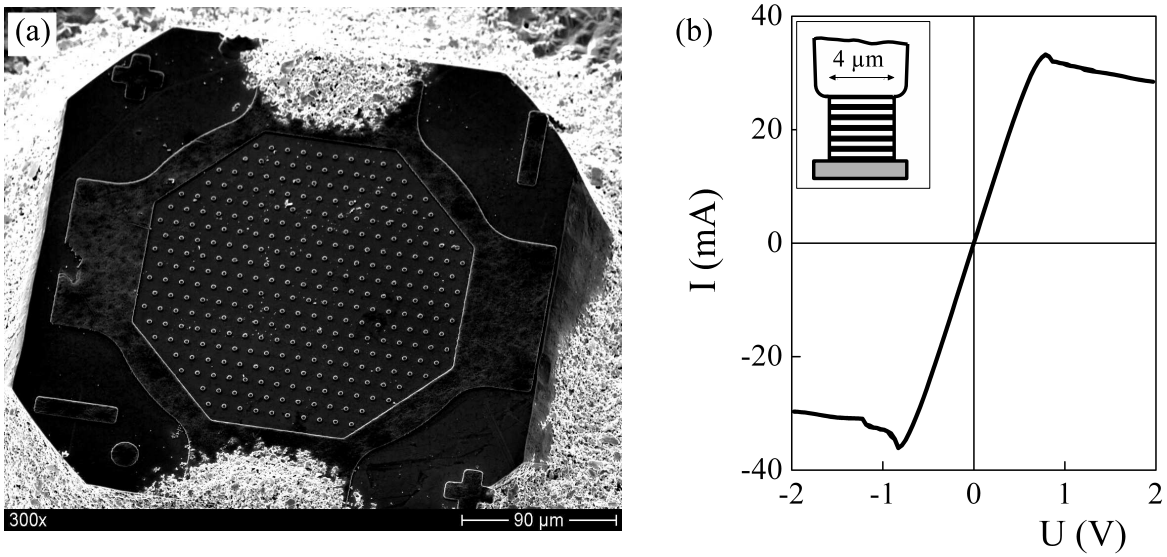

Figure 4.4: A single superlatice device, as used in the modified SPO, carried about 200 superlattice mesas; the large superlattice structure surrounding the mesa array allowed to contact the superlattice mesas from the bottom (a). Current-voltage curve of the superlattice device with a single mesa contacted (diameter of 4 μm) (b). Schematic of a single superlattice mesa contacted by a whisker antenna (b), inset.

a nonlinear behavior. The curve was almost antisymmetric and showed an ohmic behavior at small voltage. If a critical voltage of 0.8 V was exceeded, the current decreased with increasing voltage. In addition to the ohmic resistance of the superlattice ($R_0 \sim 5\ \Omega$), a series resistance ($\sim 10\ \Omega$) occurred, which originated mainly from the contact between the top n-$GaAs$ layer and the $Ni/Ge/Au$ alloy.

4.3 Experimental setup

Pump radiation source

The SPO was pumped with a frequency synthesizer which delivered a maximal power of 4 mW in a frequency range from 75 GHz to 110 GHz. The power was adjustable in steps of 0.02 dB. The radiation was guided to the SPO via an isolator which prevented reflection of radiation to the radiation source. For the modified SPO, an amplifier which delivered up to 50 mW was used between synthesizer and SPO.

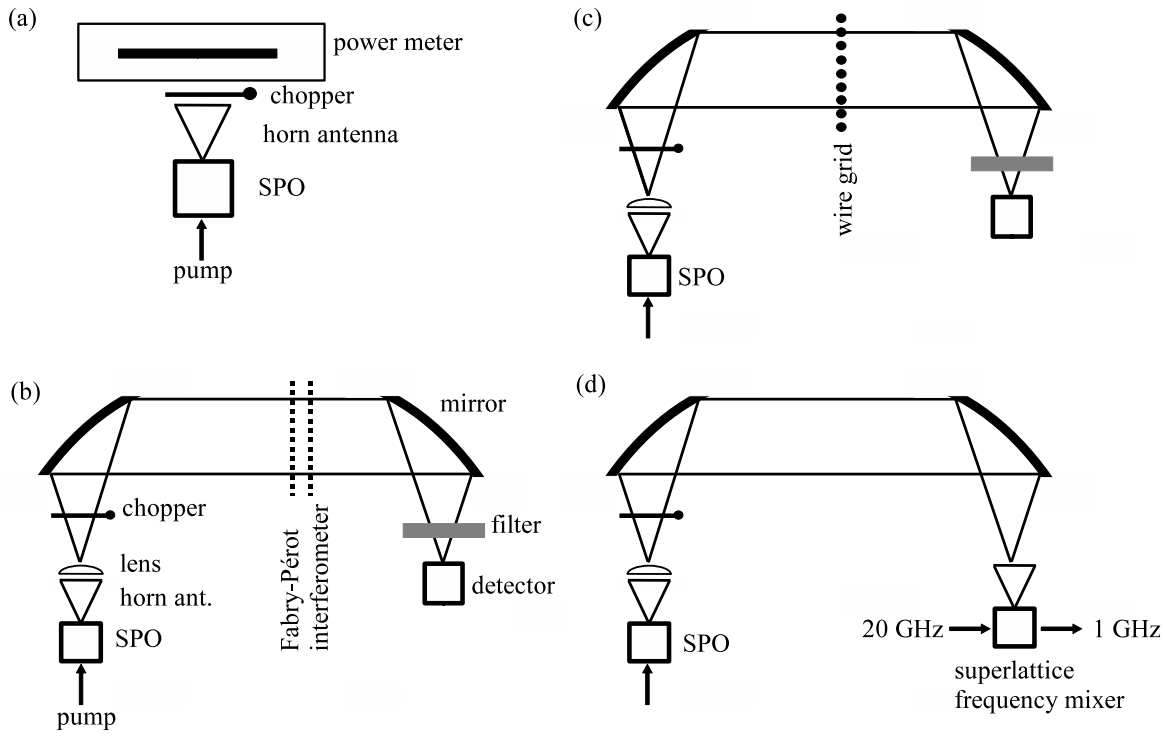

Figure 4.5: Schematics of measurement setups for power measurement (a), for Fabry-Perot interferometry (b), with a wire grid reflector forming an external resonator coupled to the SPO (c) and for detection with a superlattice frequency mixer.

Detection

The beam from the SPO was made parallel by off-axis parabolic gold mirrors and focused, by a second, similar mirror, onto a detector (fig. 4.5). As detector, either a Golay cell or a Bolometer was used. The Golay cell (noise equivalent power NEP $\sim 10^{-10}$ WHz$^{-1/2}$) was operated at room temperature; the bolometer (NEP $\sim 10^{-13}$ WHz$^{-1/2}$) was cooled down to ~ 2 K with liquid helium. With the chosen filters, the bolometer was suitable to detect radiation from 50 GHz to 6 THz. The signals from the detectors were measured with a lock-in amplifier. In order to modulate the signal from the SPO, an optical chopper was placed into the beam directly in front of the SPO.

Power measurement

The power of the emission from the SPO was measured with a terahertz power meter (Thomas Keating Ltd, UK) (fig. 4.5 a). The power meter contains an air-cell (diameter of sensitive area ~ 3 cm) and a pressure-transducer. The radiation from the SPO was

modulated with a chopper (frequency 30 Hz) which was placed between SPO and power meter. The distance between horn antenna aperture and the air-cell was about four centimeter.

Fabry-Perot interferometry

A Fabry-Perot interferometer with metal-meshes [33] was used to analyze the spectrum of the SPO. The Fabry-Perot interferometer was placed into the parallel beam (fig. 4.5 b). It consisted of two parallel metal meshes (mesh period 50 μm, thickness 6 μm) which formed the Fabry-Perot resonator. The distance between the meshes could be varied in steps of 1 μm. The quality of the Fabry-Perot resonator was of the order of 100. The formation of standing waves, either between SPO and Fabry-Perot interferometer, or between Fabry-Perot interferometer and detector could be suppressed by sheets of polymer foam, which damped the signal by a factor of about twenty.

In the course of the experiments, the Fabry-Perot setup was improved: Using the Bolometer instead of the Golay cell resulted in a much higher sensitivity of the detector. A box was built around the interferometer which prevented air motion at the metal meshes, reducing disturbances to a minimum. For radiation at a frequency of 300 GHz, a change in the mesh distance due to moving air by 1 μm results, in a change of the transmission frequency of 300 MHz. This is about half the width of the Fabry-Perot transmission curve. Finally, the detection circuit was electrically shielded. These measures made the Fabry-Perot setup suitable for the detection of weak terahertz signals.

Partial reflector

The impedance mismatch at the connection between resonator waveguide and horn antenna, which formed a partial reflector (see fig. 4.1), defined the output coupling from the resonator. For a first investigation of the influence of output coupling on the SPO, the reflectivity at the mismatch was varied by changing the position of the horn antenna relative to the waveguide.

External resonator

An external resonator, that was coupled to the waveguide resonator inside the SPO was realized with a wire grid in the parallel beam (fig. 4.5 c). The wire grid was placed in the parallel beam with the plane that was formed by the wires perpendicular to the beam direction. By rotating the wire grid and thereby the direction of the wires relative to the polarization direction of the radiation, the transmissivity of the wire grid was variable continuously between zero and one. This allowed to adjust the output coupling of the coupled-resonator system. The distance between SPO and wire grid was 1.5 m; the eigenfrequencies of a resonator of length $L_{res} = 1.5$ m are expected to have a distance of $\Delta\nu = \frac{c}{2L_{res}} = 100$ MHz, where c is the speed of light.

Superlattice frequency mixer

By means of a superlattice frequency mixer [34], the signal from the SPO was converted to a low frequency ($\sim 1\ GHz$), where it could be detected with a spectrum analyzer (fig. 4.5 d). The mixer worked with two quasi planar superlattice devices. The signal of the SPO was mixed with the 20^{th} harmonic of a signal (frequency ~ 20 GHz) from a frequency synthesizer. The frequency difference between the SPO signal and the 20^{th} harmonic was ~ 1 GHz. The frequency mixing was due to the nonlinear miniband transport in the superlattice.

5 Experimental results

5.1 SPO spectrum

The Fabry-Perot interferogram (fig. 5.1) shows peaks with a separation of about 500 μm, corresponding to half the wavelength of third harmonic radiation at a frequency of 300 GHz. The emission from the SPO consisted mainly of third harmonic radiation. Peaks from the fifth and seventh harmonic occurred, but were smaller by almost two orders of magnitude compared to peaks from the third harmonic.

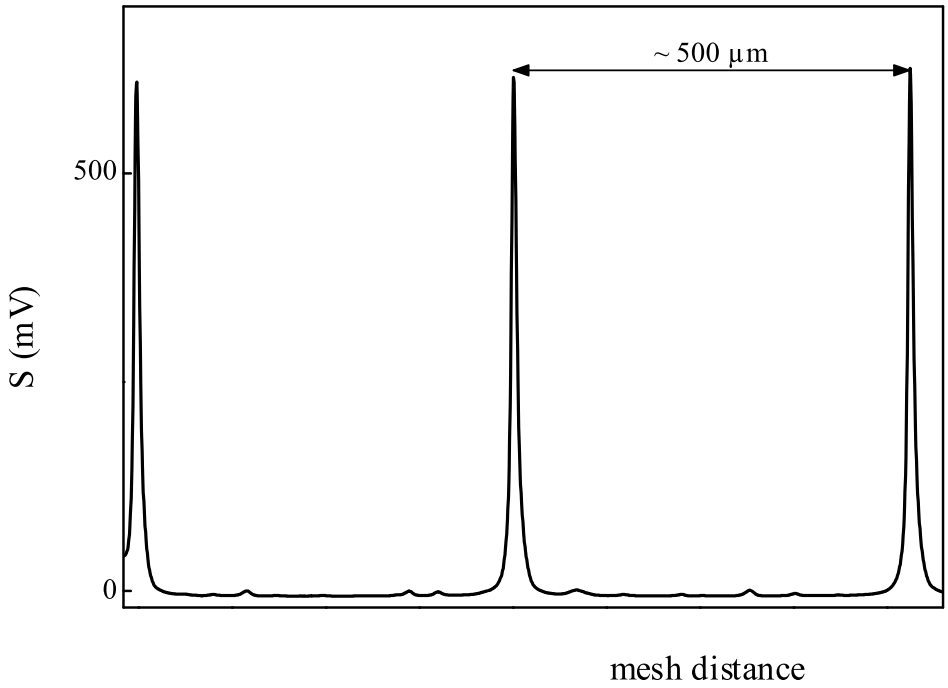

Figure 5.1: Fabry-Perot interferogram, detected with a Golay cell. Higher harmonic signals are weaker by at least a factor of hundred compared to the third harmonic signal. The distance of $\sim 500\,\mu$m corresponds to half the wavelength of 300 GHz radiation.

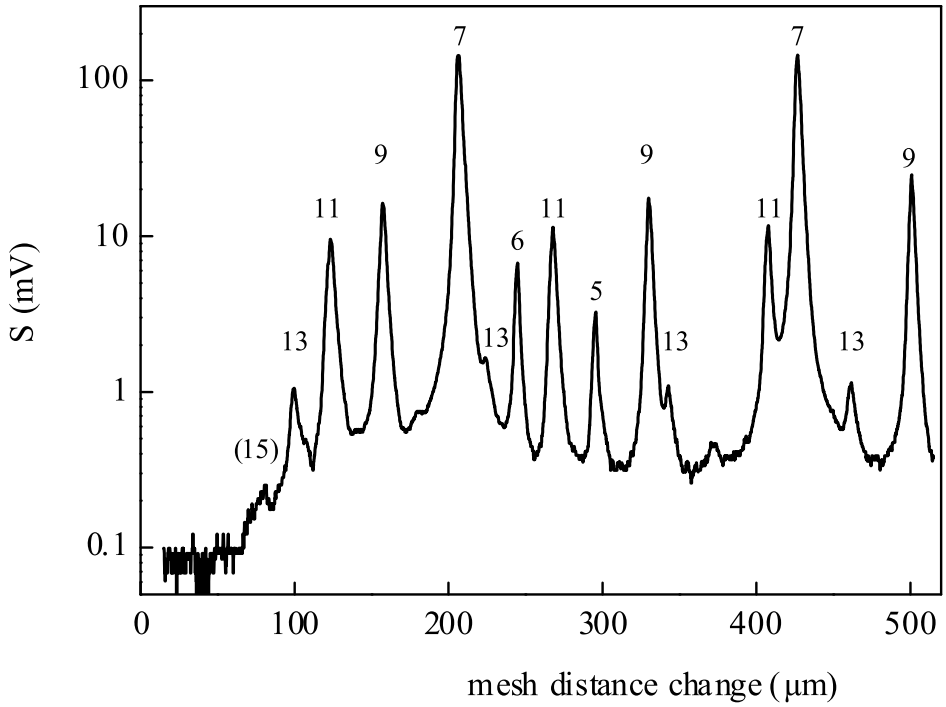

Figure 5.2: Fabry-Perot interferogram showing high harmonics from an SPO up to the fifteenth.

Detection of high harmonics

An interferogram which was obtained with the improved Fabry-Perot setup with the bolometer is depicted in figure 5.2. Signals below 500 GHz were suppressed by a waveguide filter. Peaks from all odd harmonics up to the thirteenth (~ 1.3 THz) were identified. The peak from the sixth harmonic is a sign for a minor asymmetry of the superlattice. The peaks occurred periodically according to half the wavelength of each harmonic. The first peak ($S \sim 0.4$ mV) in the interferogram corresponds most probably to the fifteenth harmonic. Higher harmonics may have been absorbed by water vapor. The existence of such high harmonics indicates that the nonlinear miniband electron transport in our superlattice works up to terahertz frequencies.

5.2 Threshold behavior

A first sign for parametric oscillation was a threshold-like behavior of the third harmonic signal S_3 (fig. 5.3). With increasing pump power P_1, the third harmonic signal S_3 increased as P_1^3. When a critical pump power $P_c \sim 1$ mW was exceeded, S_3 showed a

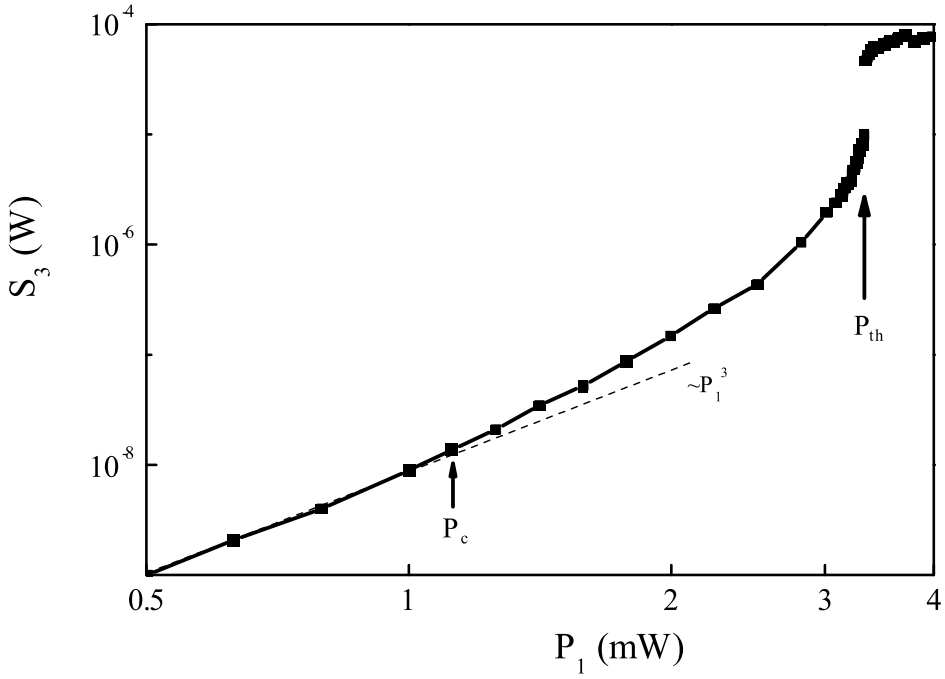

Figure 5.3: Threshold behavior of the SPO: a jump in the third harmonic signal occurs when the threshold pump power P_{th} is reached, indicating the onset of parametric oscillation.

stronger increase. A threshold-like increase by almost one order of magnitude occurred at a threshold pump power P_{th}. At a further increase of the pump power, the signal saturated. The critical pump power P_c can be attributed to a pump power where the pump voltage amplitude ($\hat{U}_1$) is equal to the critical voltage (U_c) of the superlattice. Accordingly, the signal at low pump power is due to conventional frequency multiplication. At a pump power between P_c and P_{th}, the signal is caused by frequency multiplication without parametric oscillation, most probably mediated by the formation and annihilation of space charge domains [26, 0]. At pump powers above P_{th}, the SPO signal is due to parametric oscillation. When P_1 is further increased the signal keeps almost constant and decreases at higher P_1. The saturation of the signal is in agreement with the theoretical treatment (see fig 3.8), the third harmonic power is limited by the peak current of the superlattice.

5.3 Feedback

A variation of the reflectivity at the mismatch between third harmonic resonator and horn antenna changed the threshold behavior of the SPO (fig. 5.4). The dependence

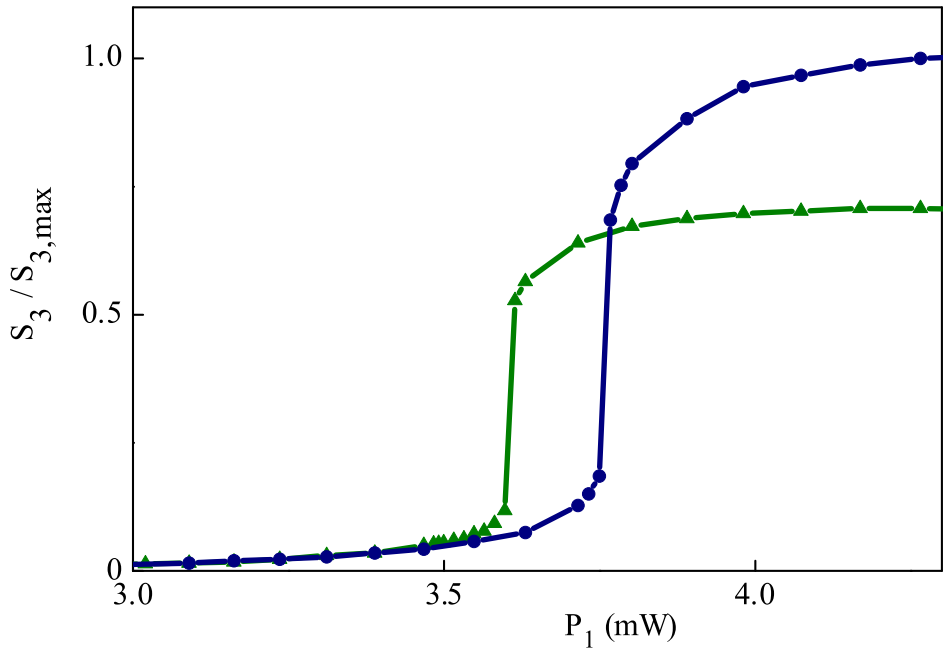

Figure 5.4: Dependence of the third harmonic signal on the pump power. The position of the horn antenna relative to the resonator waveguide is shifted which changes the output coupling. A higher output coupling results in an increase of P_{th} and of the third harmonic signal S_3.

of the third harmonic signal S_3 on the pump power was measured for two different positions of the horn antenna relative to the resonator waveguide. At high output coupling, S_3 saturated at a maximal value $S_{3,max}$. A decrease of the output coupling resulted in a decrease of S_3 ($S_3/S_{3,max} \sim 0.7$). The corresponding pump threshold decreased from 3.73 mW to 3.58 mW. The dependence of P_{th} on the output coupling was an indication for the necessity of feedback for SPO operation.

5.4 Power and conversion efficiency

For measuring the power P_3 of the SPO, the position of the horn antenna relative to the resonator waveguide was adjusted for maximal signal. The power of the SPO was about 0.1 mW$\pm$0.02 mW. The corresponding conversion efficiency of the SPO was $\sim$ 2.5 percent (pump power 4 mW). Taking into account the damping by the isolator ($\sim$ 2 dB) and losses due to the series resistances in the superlattice device ($\sim$ 5 dB), the conversion efficiency of the superlattice itself was about 8 percent.

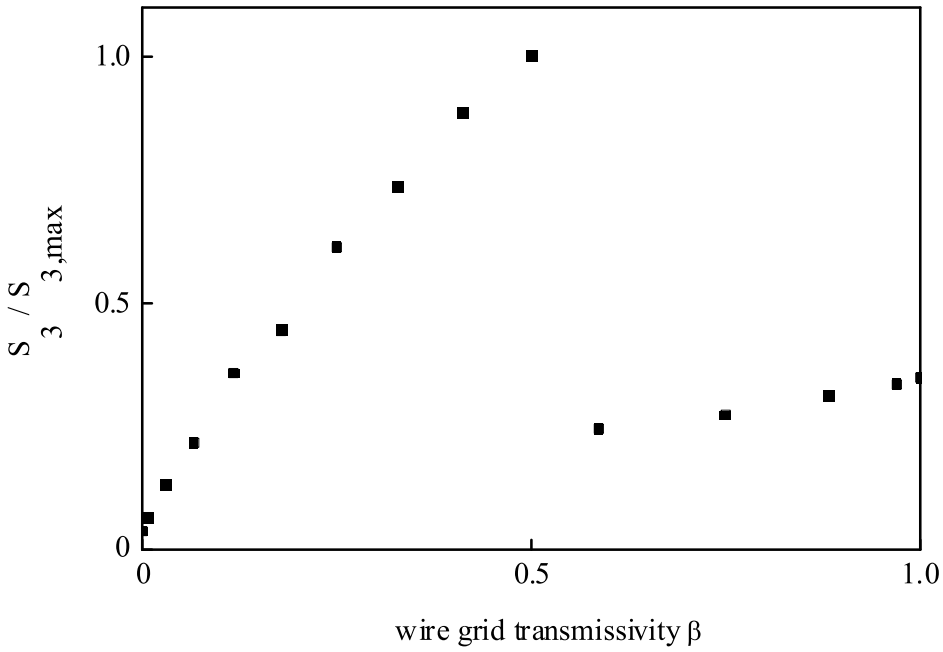

Figure 5.5: Dependence of the third harmonic signal on the output coupling of an external resonator (between a rotatable wire grid and the mismatch), coupled to the SPO. Oscillation is switched off when too much power is coupled out.

5.5 Optimum output coupling

The third harmonic signal S_3 was measured while the wire grid was rotated changing its transmissivity β from almost zero to almost one (fig. 5.5). The pump power was close to P_{th}. Starting from $\beta = 0$, the signal increased sublinearly. When a threshold wire grid transmissivity β_{th} was exceeded, the signal decreased abruptly by more than two third. Feedback was too low to sustain oscillation. The remaining signal was due to frequency multiplication (see fig. 5.3). The output power of the SPO could be optimized by adjusting the output coupling to an optimum value (β_{th}) close to the break down of oscillation. This behavior is known from other oscillators.

5.6 Starting behavior with an external resonator

The influence of feedback from an external resonator on the onset of oscillation was studied. An external resonator between horn antenna and wire grid (transmissivity β adjusted to ~ 0.5) formed a coupled resonator together with the waveguide resonator. While S_3 was detected with a Golay cell, the pump frequency was varied, resulting in a frequency sweep of the third harmonic within a range of ~ 500 MHz. The frequency

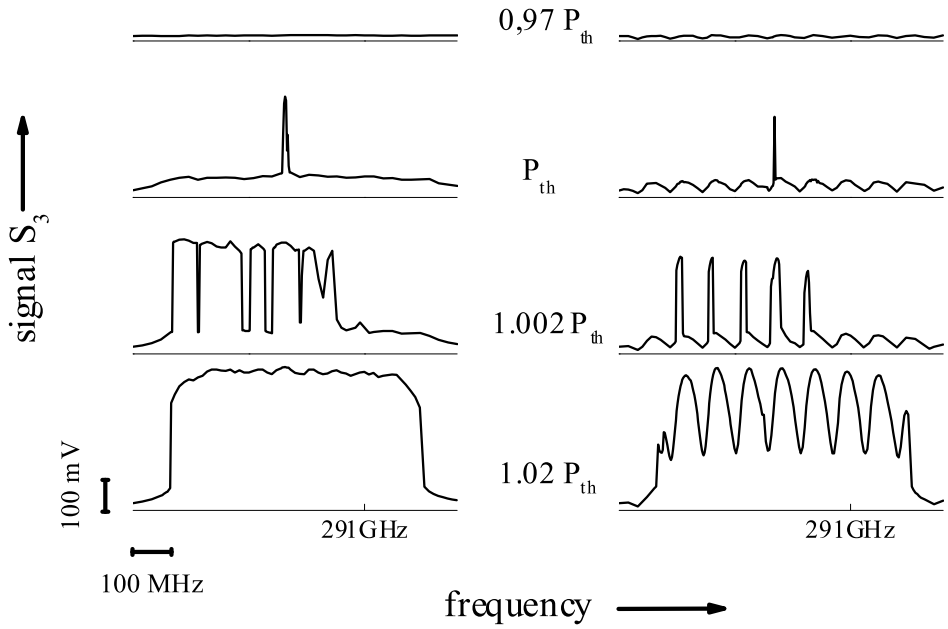

Figure 5.6: Influence of feedback from an external resonator on the onset of oscillation. Frequency characteristic for different pump powers close to threshold pump power without (left) an with (right) external resonator.

sweep was carried out with four different pump powers close to the threshold pump power: $P_1 = 0.97P_{th}$, $P_1 = P_{th}$, $P_1 = 1.002P_{th}$ and $P_1 = 1.02P_{th}$. Without the external resonator (fig. 5.6, left side), the signal was constant for pump powers below P_{th}. At $P_1 = P_{th}$, oscillation occurred within a narrow frequency range (~ 0.3 percent of the center frequency) which can be attributed to an eigenfrequency of the waveguide resonator. With P_1 slightly above P_{th}, the range where oscillations occurred broadened but still was discontinuous, which was due to slightly different pump power levels at different frequencies. At higher pump power, oscillations could be detected within the whole frequency range. The limitation of the frequency range to about 500 MHz is due to resonances in the pump waveguide (see fig. 5.8). With the external resonator (fig. 5.6, right side), the signal for $P_1 < P_{th}$ shows a weak ripple according to the transmission of the external resonator and a single peak from the internal resonator at $P_1 = P_{th}$. When P_1 was increased slightly above P_{th}, oscillations developed only in narrow frequency intervals, separated by 100 MHz, corresponding to the eigenfrequencies of the external resonator. With increasing pump power, the ranges of oscillation broadened and finally overlapped. A decrease of the wire grid transmissivity from 0.5 to 0.1 resulted in a small decrease (~ 1 percent) of P_{th}. The effect was small because in

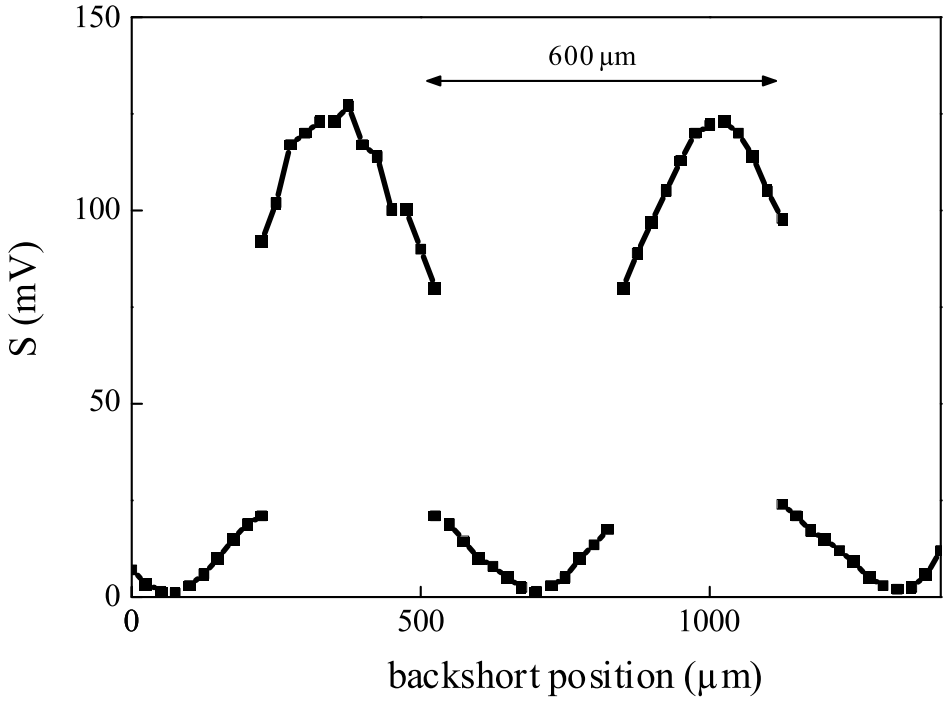

Figure 5.7: SPO signal for varying resonator length

our setup only a portion of the radiation was coupled out from the waveguide resonator to the external resonator.

5.7 Variation of the resonator length

The third harmonic signal S_3 of the modified SPO was measured while the position of the backshort in the resonator was varied (fig. 5.7). The pump power was adjusted close to the threshold pump power. The oscillator could be switched on and off. The distance between the backshort positions where the oscillator was switched on (or off, respectively), was 0.6 mm which is in good agreement with half a wavelength in the resonator. The experiment demonstrates the phase sensitivity of the oscillator with respect to feedback. However, the ranges of oscillation are relatively broad, indicating gain even if the phase of the feedback is not optimal.

5.8 Broadband tunability

While the pump frequency was varied from 75 GHz to almost 96 GHz, the SPO delivered a continuous signal (fig. 5.8) from 235 GHz to 288 GHz. The signal strength

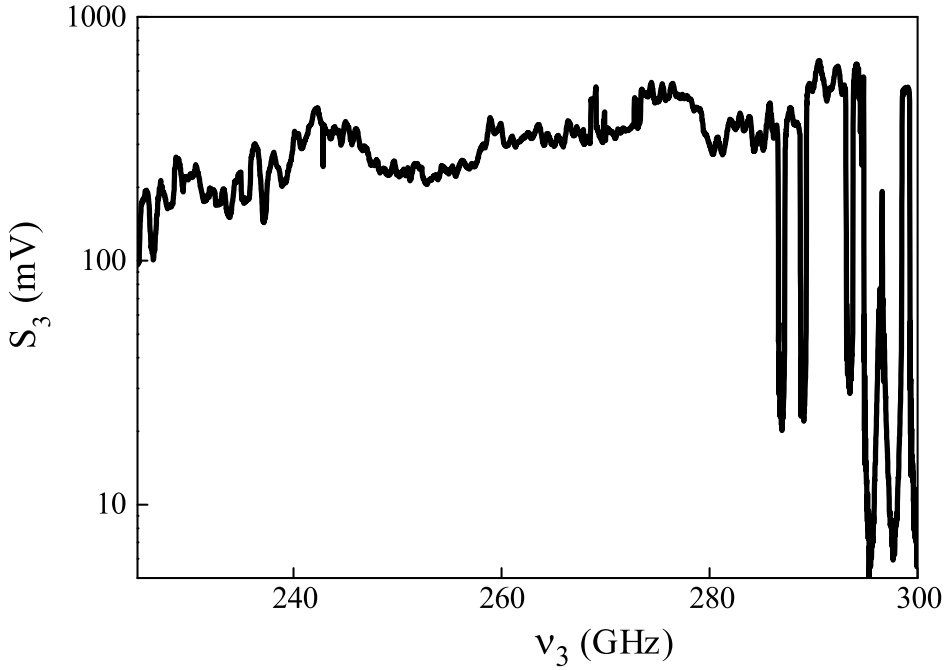

Figure 5.8: The oscillation frequency was continuously tunable from $235\,GHz$ to $288\,GHz$, simply by changing the pump frequency.

slightly increased with increasing frequency. At the upper edge of the frequency range, resonances, most probably in the pump waveguide, became visible. For frequency above 100 GHz, the pump power from the frequency synthesizer decreased with increasing frequency. With a higher pump power available, the frequency range of continuous operation would have been larger.

5.9 Monochromatic radiation source

The signal of the SPO (fig. 5.9) was detected with a superlattice frequency mixer and a spectrum analyzer. The picture shows a peak with a full width at half maximum of about 15 kHz. The signal from the SPO was much more narrow, most probably three times as broad as the pump signal. The peak was broadened due to the resolution bandwidth ($\sim$ 10 kHz) of the spectrum analyzer. The broad background signal was caused by the frequency synthesizer used in the pump source and in the frequency synthesizer used to generate the local oscillator signal for the mixer.

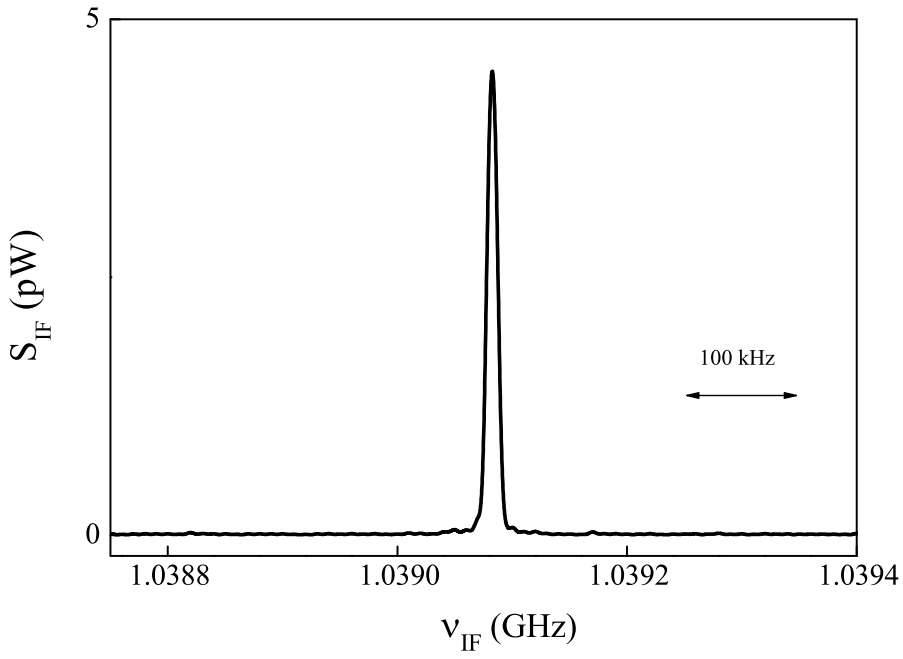

Figure 5.9: SPO signal detected with a superlattice mixer in 16^{th} harmonic order.

5.10 Discussion

The experimental results show that feedback is an important part of the SPO mechanism. The threshold like onset of the signal, the influence of feedback on the threshold pump power and on the onset of oscillation and the existence of an optimum output coupling confirm the model of parametric oscillation which has been developed in the theoretical treatment.

The frequency tunability over a wide frequency range at almost constant power without an adjustment of the third harmonic resonator shows that the superlattice in an SPO is able to adjust itself to the surrounding resonator system. It further indicates that it should be possible to extend the operation frequency range of an SPO to higher frequencies. By use of a pump source between 300 GHz and 400 GHz, radiation at terahertz frequencies could be generated.

In the theoretical description it has been assumed that the electric field distribution in the superlattice in an SPO is homogeneous. A high frequency field which acts on a superlattice may either lead to a domain or to a single-electron nonequilibrium state. In the domain state, a subterahertz field interacts with transient electron ensembles

[26, 35, 36]. A pump field creates and annihilates, during each half cycle, a space charge domain, giving rise to a current that is the source of third harmonic radiation. It can not be excluded that space charge domains occurred in the SPO. The formation of space charge domains might prevent the occurrence of gain [37]. In a single electron state, the electric field within the active superlattice remains uniform and the electrons interact independently from each other with the field. In order to prevent the formation of space charge domains, the pump frequency ω_1 has to be large compared to the domain buildup frequency $\omega_D = 2\pi/\tau_D$, where τ_D is the time a space charge domain needs to build up. τ_D is of the order of the dielectric relaxation time. According to [37], there is still gain even if space charge domains occur. For an exemplary superlattice discussed in [37], gain was, in spite of the formation of domains, decreased by only ten percent for a relatively low pump frequency $\omega_1 = 0.1\,\omega_D$. For the superlattice with $\Delta \sim 140$ meV, the dielectric relaxation time is about 1.1 THz. Therefore it is probable that in our modified SPO there was enough gain for parametric oscillation, even if domains occurred. However, both SPOs showed similar behavior.

For an SPO operated at terahertz frequencies, the electric field distribution would most probably be homogeneous as supposed in the theoretical treatment.

6 Prospects of microwave-pumped superlattice THz radiation sources

The theoretical treatment of the SPO, with results that are in agreement with our experiments in the subterahertz frequency range, is now applied to terahertz frequencies.

6.1 Terahertz SPO

6.1.1 Optimum operation conditions of a 3 THz SPO

In this section, the operation conditions of a terahertz SPO [38] are studied. The SPO is pumped at a frequency $\nu_1 = \omega_1/2\pi = 1$ THz and oscillates at $\nu_3 = \omega_3/2\pi = 3$ THz (corresponding to $\omega_3\tau = 3$). The third harmonic resistance R_3, the pump resistance R_1 and the efficiency η_{31} for conversion of pump to third harmonic radiation were calculated as a function of the pump voltage amplitude $\hat{U}_1$ and the third harmonic amplitude $\hat{U}_3$.

Figure 6.1 gives a survey of the results for the SPO. There are regimes of loss (hatched areas) and of gain (white). The third harmonic resistance R_3 (fig. 6.1, top) depends nonlinearly on the pump and the third harmonic amplitude. For small $\hat{U}_3$, R_3 is negative for pump voltages larger than a threshold pump voltage amplitude $\hat{U}_{1,th}$. For a fix $\hat{U}_1 > \hat{U}_{1,th}$, the absolute value of R_3 increases for increasing $\hat{U}_3$ (from zero for $\hat{U}_3 = 0$) and becomes infinite at the border of the range of negative R_3. The pump resistance R_1 (fig. 6.1, center) depends also nonlinearly on $\hat{U}_1$ and $\hat{U}_3$, but the dependence is completely different compared to that of R_3. In the range we considered, the pump resistance R_1 is always positive and has finite values. It varies much less than R_3. The hatched area in the graph refers to the range where R_3 is positive. The efficiency η_{31} (fig. 6.1, bottom) depends strongly on both $\hat{U}_1$ and $\hat{U}_3$ and shows two maxima in the range of amplitudes that has been studied. An efficiency of 13 percent is reached at a pump amplitude of $5\,U_c$ while at $U_1 \sim 9\,U_c$, an efficiency of 23 percent

is obtained.

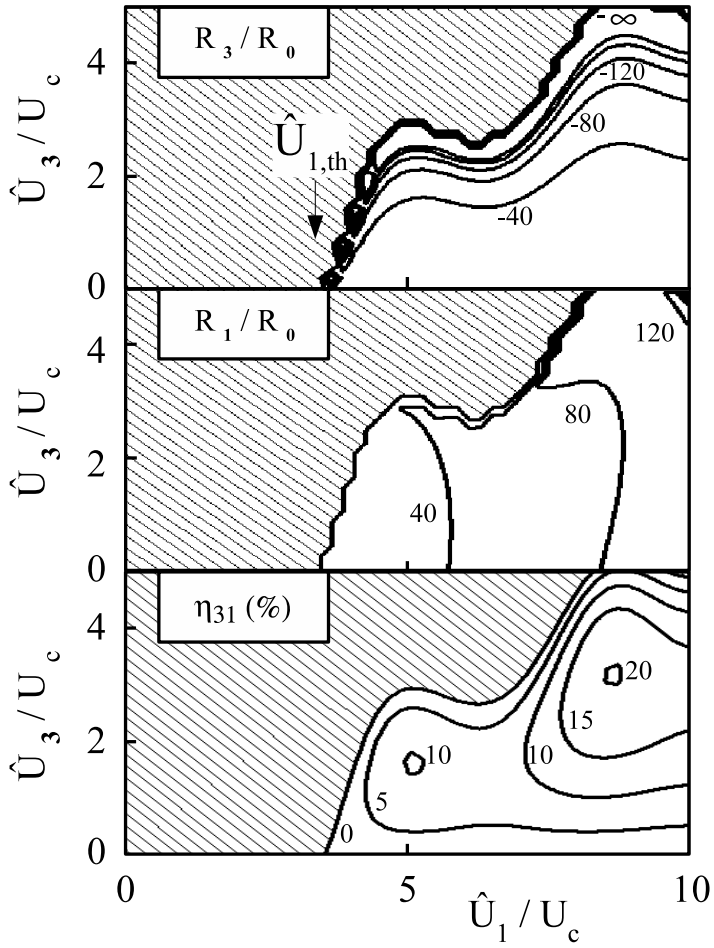

Figure 6.1: Third harmonic resistance R_3, pump resistance R_1 and Conversion efficiency η_{31} of a terahertz SPO (1 THz $\rightarrow$ 3 THz) for different pump and third harmonic amplitudes. Conversion efficiencies of 13 percent and 23 percent are obtained at two separate maxima.

To specify the operation conditions of an SPO at 3 THz, R_3, R_1 and η_{31} have been calculated for varying $\hat{U}_3$ (fig. 6.2). A pump voltage $\hat{U}_1 = 5\,U_c$, at which the first maximum of the efficiency occurred, has been chosen. The absolute value of the negative resistance R_3 increases with increasing $\hat{U}_3$ and becomes infinite before switching to the positive resistance range, where loss for third harmonic radiation prevails. In the same range, R_1 increases only slightly. The efficiency increases linearly at small $\hat{U}_3$ and then reaches its maximum value. A portion ($\eta_{31} = 0.1$) of the pump radiation is converted to third harmonic radiation while the main portion (~ 0.9) of the pump radiation is dissipated.

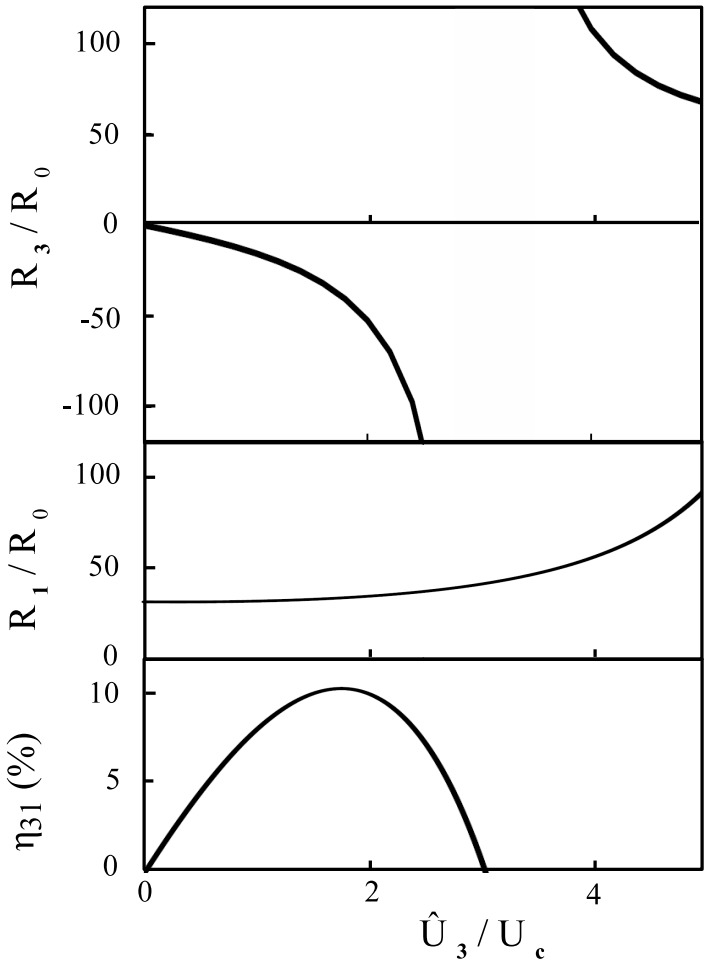

Figure 6.2: Third harmonic resistance, pump resistance and conversion efficiency for an SPO operating at 3 THz for different third harmonic amplitudes. The pump voltage ($\hat{U}_1 = 5\,U_c$) is close to the first optimum.

6.1.2 Maximum operation frequency

In a further calculation (fig. 6.3), the dependence of the threshold pump voltage $\hat{U}_{1,th}$ on the oscillation frequency ν_3 of the SPO was determined. For frequencies for which $\omega\tau \leq 1$, the threshold is $\hat{U}_{1,th} \sim U_c$; at higher frequencies $\omega\tau > 1$, $\hat{U}_{1,th}$ increases almost linearly with the frequency ν_3. The calculation was performed for a small third harmonic amplitude ($\hat{U}_3 \sim 0.1\,U_c$). At the frequency $\nu_{3,max}$, the mobility switches from negative (gain) to positive (loss) values. As the third harmonic resistance R_3 has to be equal to the resonator resistance, which is usually of the order of some hundred ohms, a realistic oscillation frequency would be lower than $\nu_{3,max}$. At small third harmonic amplitude, gain is present even if the pump voltage does not exceed the critical voltage

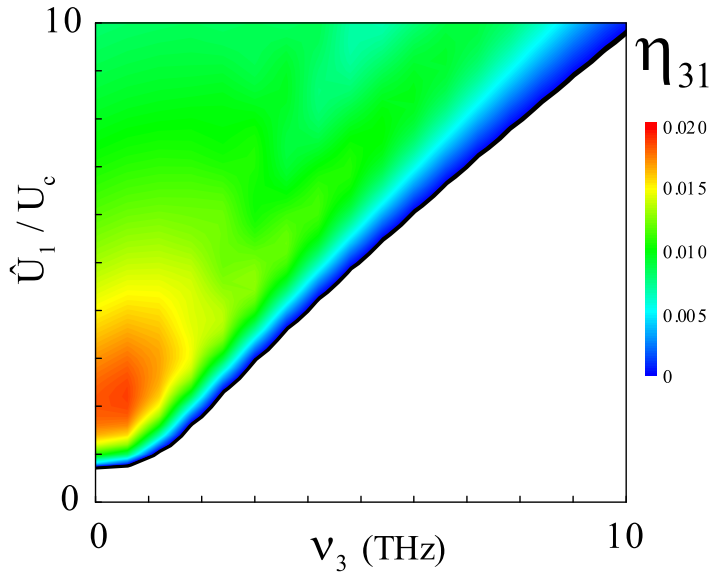

Figure 6.3: Dependence of the conversion efficiency η_{31} of a third harmonic SPO on the pump amplitude and the third harmonic frequency ($\hat{U}_3 = 0.1\ U_c$). In the white region, the superlattice absorbs radiation. Gain (colored area) for third harmonic radiation at 10 THz can be obtained with a pump voltage amplitude of about 10 U_c.

of the superlattice. This effect is very weak; in order to obtain gain at stronger third harmonic voltages, the regime of negative differential mobility has to be reached, i.e., $\hat{U}_1$ has to be larger than U_c.

6.1.3 Discussion

With the results, the optimum operation conditions for an SPO with our superlattice ($R_0 \sim 12\ \Omega$) can be determined. For operation with maximum efficiency at $\hat{U}_1 = 5\,U_c$, $\hat{U}_3$ has to be about $1.8\,U_c$. Under these conditions, the superlattice would have a pump resistance $R_1 \sim 350\ \Omega$ and a third harmonic resistance $R_3 \sim 600\,\Omega$. Pump circuit and third harmonic resonator circuit have to be matched to these values for optimal operation, which is feasible. In case the resonator circuit is not optimally matched to the superlattice, the feedback from the resonator to the superlattice occurs in such a way that $\hat{U}_3$ is appropriately adjusted, i.e., the superlattice matches itself to the resonator circuit. This can be concluded from figure 6.1, top; during switching on the pump voltage, joint with an increase of $\hat{U}_1$, the third harmonic field is built up while the superlattice resistance R_3 follows a contour line for a value that is equal to the resistance of the resonator. All contour lines have their origin in one point, where $\hat{U}_3$

is equal to zero. Thus, in principle, the superlattice matches itself to any resonator resistance. The oscillation can be started by frequency multiplication according to the nonlinear electron transport without the involvement of feedback.

The high frequency pump voltages that were discussed had voltage amplitudes (corresponding to electric field amplitudes up to 100 kV/cm) that are smaller than the strengths of the static voltage which a superlattice can withstand without being destroyed by heating effects.

The spatial extension of the trajectory of a Bloch oscillating electron, $\xi_0 = \frac{\Delta a}{\hbar\omega_B} = \frac{\Delta L}{eU_s}$ depends on the static voltage U_s applied to a superlattice of the length L. With increasing voltage, ξ_0 decreases. When an electron trajectory is confined to one superlattice period ($\xi_0 = a$), the miniband picture is not valid any more.

For our superlattice in the quasiplanar design (miniband width $\Delta \sim 25$ meV), the trajectory of an electron extends over one superlattice period if a static voltage of $6\,U_c$ is applied. According to the calculation depicted in figure 6.3, a maximal oscillation frequency $\nu_{3,max}$ of about 6 THz can be obtained. With the superlattice in mesa design which has a much larger miniband width ($\Delta \sim 140$ meV), much higher voltages can in principle be applied resulting in a theoretical frequency limit of about 30 THz.

Another limit of the operation frequency is the capacitance that is formed between the top contact layer of the superlattice and the highly doped substrate, which may short-circuit the superlattice with respect to high frequency currents. As the resistance of the capacitor ($X_c = 1/\omega C$) depends on the frequency of the current, one can roughly estimate a frequency limit for which the capacitive resistance equals the resistance of the superlattice (200 Ω to 400 Ω for optimum operation at 3 THz). For both superlattice devices we have used in the SPOs, the frequency limit is around 3 THz. In order to push the limit to higher frequency, the resistance of the superlattice can be reduced by increasing the miniband width or the doping level.

In the calculation, it has been assumed that the field distribution inside the superlattice is homogeneous. An inhomogeneous field, joint with a charge density domain, may hinder the occurrence of gain [37] and therefore also of SPO action. Domain formation may be avoided by appropriate choice of the amplitude $\hat{U}_1$ and by making use of a superlattice with a domain transit frequency that is low compared to $\omega_1/2\pi$.

A challenge that has to be met for the realization of a terahertz SPO is the practical

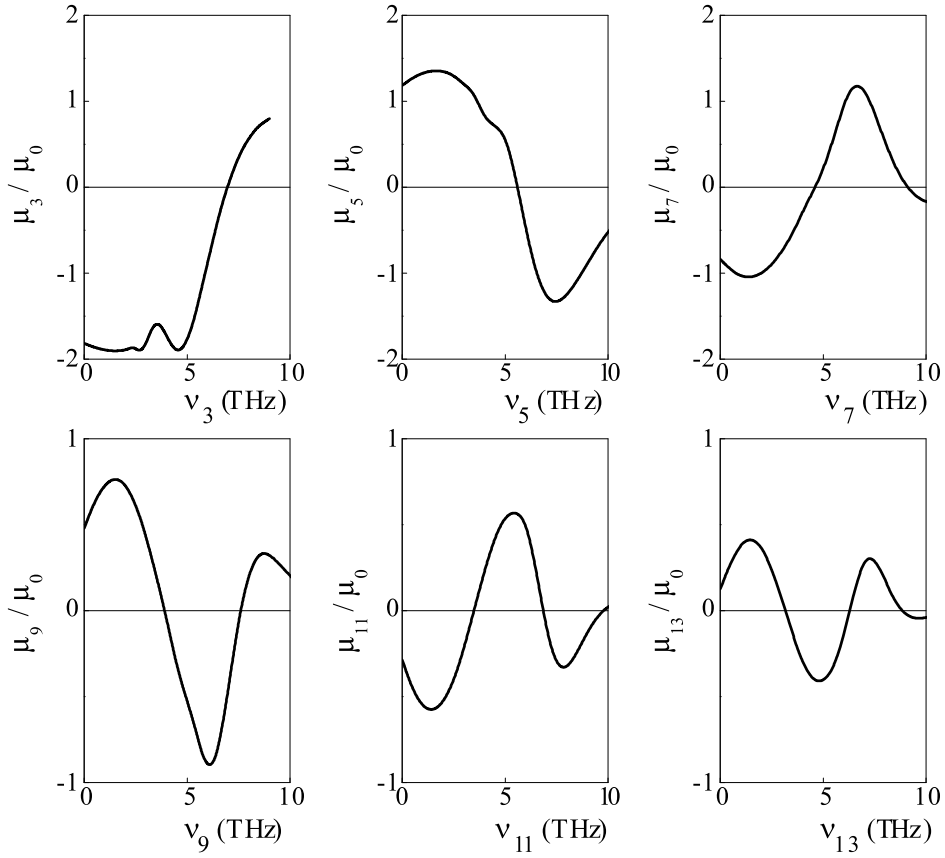

Figure 6.4: Dependence of the harmonic power of an SPO on the oscillation frequency for odd harmonics (third to thirteenth). A pump voltage amplitude $\hat{U}_1 = 7\,U_c$ and harmonic amplitudes $\hat{U}_i = 0.1\,U_c$ were chosen. Gain from zero frequency on is obtained for the 3^{rd}, 7^{th} and 11^{th} harmonic.

fabrication of the small resonators. Already being at the technical limits of chipping with our subterahertz-SPOs operating at 300 GHz, the resonator waveguide of a 3 THz SPO would be ten times smaller.

6.2 SPO operation at higher harmonics

An obstacle for the realization of a third harmonic terahertz SPO is the availability of a compact radiation source at 1 THz. It is desirable to reach terahertz frequencies with pump radiation sources working at frequencies as low as possible. This could be obtained with SPOs that operate in high harmonic orders.

6.2.1 Gain at higher harmonics

For a survey of the feasibility of high-harmonic SPOs, the dependence of the harmonic mobility μ_i on the oscillation frequency ν_i was calculated for all odd harmonics, from the third harmonic to the 13^{th}. The pump amplitude was chosen to be $\hat{U}_1 = 7\,U_c$, the oscillation frequency was varied from 0 THz to 10 THz. The harmonic voltage amplitude was very small ($\hat{U}_i = 0.1\,U_c$). The results of the calculations are depicted in figure 6.4. For all harmonics, there are ranges of gain ($\mu_i < 0$) and of loss ($\mu_i \geq 0$). For the third, seventh and eleventh harmonic, gain occurs from zero frequency on. The mobility remains negative up to a frequency limit of several terahertz (7 THz for the third harmonic, 4.5 THz for the seventh harmonic and 3 THz for the eleventh harmonic), where μ_i becomes positive. At higher frequency, the superlattice absorbs the harmonic radiation. The characteristics for the fifth, ninth and thirteenth harmonic are different. The mobility μ_i is positive at zero frequency. Gain occurs only at frequencies above a certain value (5^{th} harmonic: 6 THz, 9^{th} harmonic: 4 THz and 11^{th} harmonic: 4 THz). Within the frequency range that has been considered, for some harmonics (9^{th}, 13^{th}, 13^{th}), the mobility changes sign a second time at a higher frequency. The positions of the zero-points depend on the pump amplitude. An increase of the pump power results in a wider frequency range for gain. The results show that in principle it is possible to realize an SPO operating at harmonics higher than the third one. Besides the third harmonic, the seventh and thirteenth are suitable for SPO-action from zero frequency on, while at the fifth, ninth and eleventh harmonic, gain occurs only at terahertz frequencies.

Other calculations showed that gain for the seventh and the eleventh harmonic is present already from zero harmonic voltage amplitude $\hat{U}_7$ or $\hat{U}_{11}$ on. Therefore, a seventh or eleventh harmonic SPO could in principle start from very small initial signals or from noise.

6.2.2 Double-resonance superlattice parametric quintupler

A possibility to obtain SPO action at the fifth harmonic at subterahertz frequencies and low terahertz frequencies is a double resonance superlattice parametric oscillator [39]. In the double resonance SPO, a semiconductor superlattice is coupled to a resonator for

the third and the fifth harmonic of a pump frequency. In a first process, similar to an SPO, pump radiation is converted to third harmonic radiation by parametric oscillation (according to $3 \cdot \omega_1 = \omega_3$). In a second, simultaneous process, third harmonic radiation together with pump radiation is converted to fifth harmonic radiation. ($\omega_3 + 2 \cdot \omega_1 = \omega_5$).

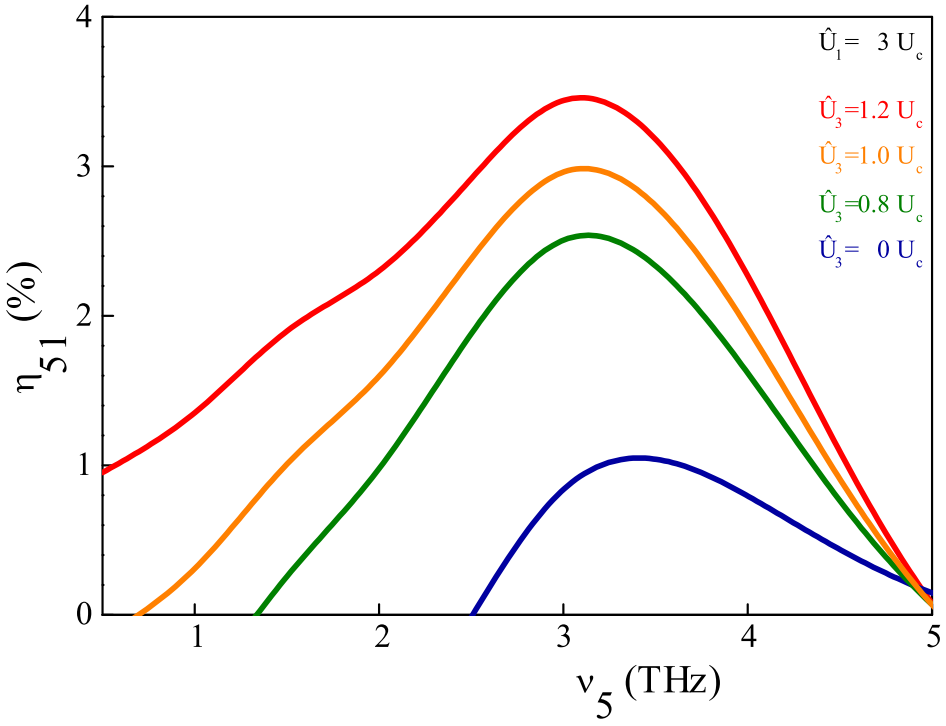

Figure 6.5: Frequency dependence of the conversion efficiency η_{51} of a quintupler for four different third harmonic amplitudes. The nonlinear interaction of third and fifth harmonic radiation with the pump radiation allows it to realize a double-resonance superlattice parametric oscillator at subterahertz and terahertz frequencies.

For the calculation of the electron drift velocity in the superlattice, a total voltage $U(t) = \hat{U}_1 \cos(\omega_1 t) + \hat{U}_3 \cos(\omega_3 t) + \hat{U}_5 \cos(\omega_5 t)$ was used. The calculation (fig. 6.5) shows the dependence of the conversion efficiency η_{51} on the oscillation frequency $\nu_5 = \omega_5/2\pi$ for different values of the third harmonic voltage amplitude $\hat{U}_3$; the pump voltage amplitude was 3 U_c. With $\hat{U}_3 = 0$, gain occurs only for frequencies $\nu_5 > 2.5$ THz with a maximum efficiency of 1 percent. With increasing $\hat{U}_3$, the range of gain extends to lower frequencies. At $\hat{U}_3 = 1 U_c$, gain extends down to 0.5 THz, with $\hat{U}_3 = 1.2\, U_c$, operation from zero frequency on is possible. With increasing $\hat{U}_3$, the maximum of the efficiency (which occurs at $\nu_5 \sim 3$ THz) increases up to ~ 3.5 percent. A double resonance SPO has been demonstrated experimentally [39] generating radiation at

frequencies of around 500 GHz.

6.2.3 Proposal of a ninth harmonic double-resonance parametric oscillator

A double resonance SPO is proposed which generates radiation at the ninth harmonic of a pump frequency using simultaneous parametric oscillation at the seventh harmonic of the pump frequency. Although there is no gain expected for the ninth harmonic at frequencies near 1 THz, by assistance of the seventh harmonic, gain for the ninth harmonic can be obtained.

The dependence of the ninth harmonic power P_9 on the ninth harmonic amplitude $\hat{U}_9$ was calculated for different seventh harmonic amplitudes $\hat{U}_7$ (fig. 6.6). The pump field $\hat{U}_1$ was chosen to be $3\,U_c$, the pump frequency was 100 GHz ($\omega_1\tau \sim 0.1$). At a seventh harmonic amplitude $\hat{U}_7 = 0$, P_9 is positive for zero ninth harmonic amplitude $\hat{U}_9$, reaches a maximum ($P_9 \sim 0.05$) and becomes negative at $\hat{U}_9 \sim 1.2\,U_c$. As gain does not occur for ninth harmonic amplitudes smaller than $1.2\,U_c$, oscillation can not start at the ninth harmonic. If an additional seventh harmonic field is present due to parametric oscillation, P_9 becomes negative at zero $\hat{U}_9$. With increasing seventh harmonic amplitude, the absolute value of the ninth harmonic power increases while the extreme value is shifted to higher ninth harmonic voltages. For $\hat{U}_7 = 2\,U_c$, P_9 has an extreme value at $U_9 \sim U_c$ where a power of almost $0.2\,P_p$ is produced, which is about 0.3 mW for our quasiplanar superlattice with $\Delta = 25$ meV. The presence of the seventh harmonic radiation makes ninth harmonic oscillation possible and the efficiency for generation of ninth harmonic radiation increases with the seventh harmonic amplitude.

6.2.4 Increased seventh harmonic efficiency by double resonance

A further analysis reveals how the efficiency for generation of seventh harmonic radiation depends on the third harmonic amplitude. The dependence of the seventh harmonic power on the seventh harmonic voltage amplitude was determined for different values of the third harmonic amplitude ($\omega_1\tau = 0.1, \hat{U}_1 = 3\,U_c$). For $\hat{U}_3 = 0$, the seventh harmonic power P_7 (fig. 6.7) was zero for $\hat{U}_7 = 0$, reached an extreme value ($\sim 0.1\,P_p$) and changed to positive values at $\hat{U}_7 \sim 1.2\,U_c$. With a third harmonic voltage $\hat{U}_3 = 1U_c$, there is no gain except in a very small range close to $\hat{U}_7 = 0$. For the same third harmonic amplitude but with opposite phase ($\hat{U}_3 = -U_c$), P_7 was increased

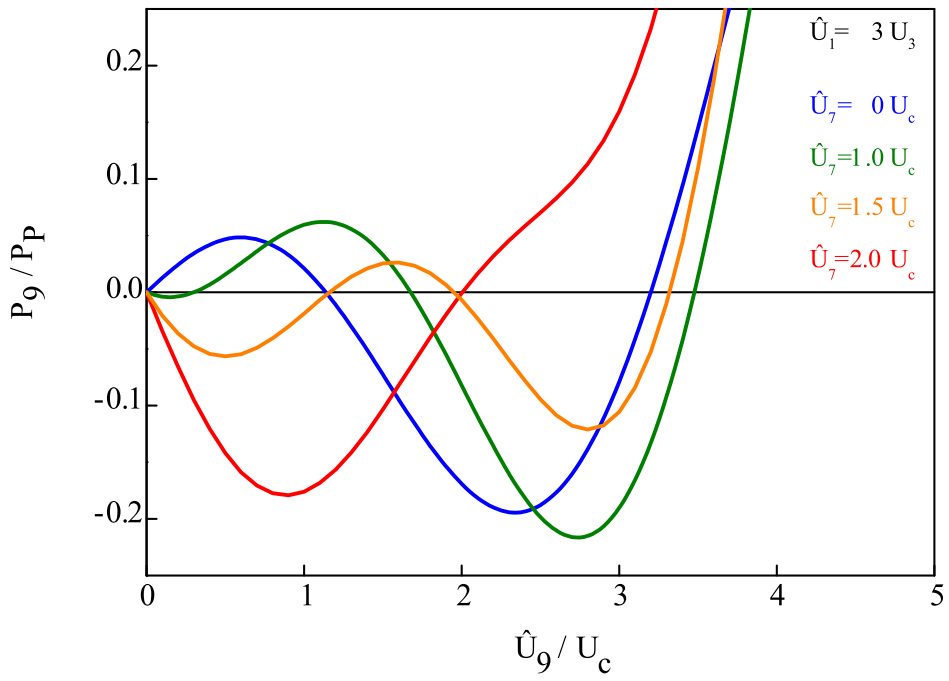

Figure 6.6: Ninth harmonic double-resonance oscillator: dependence of ninth harmonic power P_9 on the ninth harmonic amplitude $\hat{U}_9$ for different values of the seventh harmonic amplitude $\hat{U}_7$. Gain for the ninth harmonic occurs if the seventh harmonic amplitude exceeds $1\,U_c$.

by a factor of more than two. For $\hat{U}_3 = -2\,U_c$, $|P_7|$ was increased up to more than $0.4\,P_p$. The existence of a third harmonic amplitude of appropriate phase increases the seventh harmonic power significantly.

6.2.5 Discussion

The theoretical analysis showed that in principle it is possible to realize an SPO operating also at the seventh or eleventh harmonic. On the one hand, the harmonic mobility μ_i, which is a measure for the conversion efficiency decreases with increasing harmonic order. On the other hand, by making use of a high harmonic order, it is possible to realize a terahertz radiation source with a pump source at moderate frequency (e.g. 100 GHz to 200 GHz), where solid state radiation sources delivering tens of milliwatts are available.

By making use of double resonance parametric oscillations, it is possible to realize an SPO operating at a harmonic which is, in itself, not suitable for oscillation.

It is not necessary to construct a resonator waveguide with a cutoff frequency just below

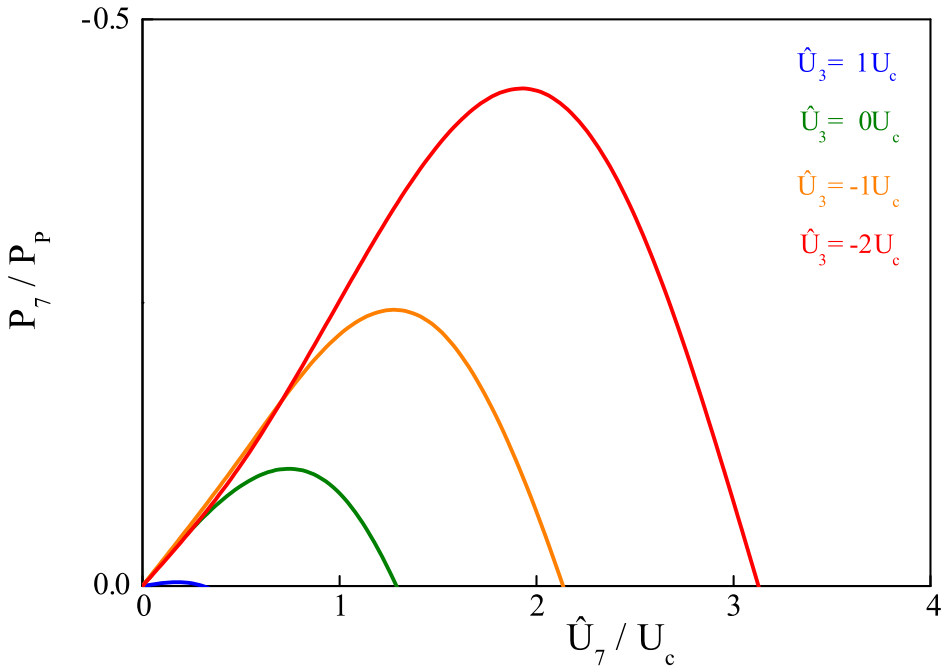

Figure 6.7: Seventh harmonic SPO. An additional oscillation at the third harmonic increases the efficiency for generation of the seventh harmonic.

the ninth harmonic frequency to build a ninth harmonic SPO. A more efficient way is to use an oversized resonator where the third, seventh and ninth harmonic can build up and to couple out only the ninth harmonic radiation through a piece of waveguide which cuts off the lower frequencies. The phase of $U_3(t)$ necessary to increase the efficiency of generation of the seventh harmonic is not optimal with regard to third harmonic SPO action. However, the calculation of the phase dependence of the third harmonic power (fig. 3.11) showed that even if the phase is off by π, the gain is reduced by only 40 percent.

The concept of the double resonance SPO, which has already been demonstrated experimentally for the fifth harmonic, might also be appropriate for other harmonics. Using an oversized waveguide resonator simplifies the construction of an SPO at high harmonic frequencies and possibly increases the conversion efficiency. The realization of a ninth harmonic SPO operating by assistance of the third and seventh harmonic would provide a terahertz radiation source which can be operated with an easily obtainable pump source.

7 Conclusion

The semiconductor superlattice parametric oscillator, a novel kind of a subterahertz and possibly terahertz radiation source, has been presented. The SPO was pumped with microwave radiation and generated third harmonic radiation by a parametric oscillation. A superlattice provided gain for third harmonic radiation.

Based on a semiclassical single electron theory for miniband transport, a description of the SPO mechanism was developed . It predicting gain for third harmonic radiation due to nonlinear miniband transport. It also predicted characteristic properties of an SPO. The optimum operation conditions of an SPO were analyzed.

In the experimental part, the first realization of an SPO was described. The SPO operated in the subterahertz frequency range. Being pumped at 100 GHz it generated radiation at 300 GHz with an efficiency of 2.5 percent (power $\sim$ 0.1 mW). A second SPO was realized which allowed it to investigate the influence of the resonator length. The experimental results confirmed that the SPO generated radiation due to parametric oscillation.

A theoretical analysis of the nonlinear electron transport in a semiconductor superlattice under the action of terahertz fields showed that an SPO is also suitable as a source of terahertz radiation. The investigation of the operation conditions of an SPO operating at three terahertz delivers a maximum conversion efficiency of 23 percent. SPO operation is theoretically possible within the whole subterahertz and terahertz frequency range.

An SPO can also be operated at higher odd harmonics, particularly at the seventh and eleventh harmonic, which allows it to easily reach the terahertz frequency range. By use of double resonance effects, where higher harmonics are generated due to the nonlinear interaction of the pump field with more than one harmonic field, SPO action can be obtained at other odd harmonics. A ninth harmonic double-resonance parametric oscillator is proposed which generates ninth harmonic radiation by assistance

of parametric oscillations at the seventh and third harmonic. Double resonance parametric oscillators can be realized with resonator waveguides of large diameter, which enormously simplifies the realization.

In conclusion, the superlattice parametric oscillator is a novel type of subterahertz and terahertz radiation source. It features desirable characteristics like compactness, operation at room temperature, coherence, broadband frequency tunability. An increase of the the output power, which is theoretically possible, will make the SPO a competitive radiation source. The possibilities that have been identified for terahertz operation at different harmonics let the SPO mechanism appear to be a promising field for future research.

8 Acknowledgment

I am indebted to many people who have directly or indirectly contributed to my work. In particular I would like to thank

- Prof. Dr. Karl F. Renk for giving me the opportunity to work on this fascinating field and for his patient guidance on my way to become a physicist.
- Ulla Turba for always having an open ear for my concerns and for her continuous ecouragement.
- The members of our working group, especially Andreas Rogl. Andi, I was fortunate to be in the same group with you. Thank you for the inspiring collaboration at work and the enjoyable times off university.
- Prof. Dr. Werner Wegscheider and Dr. Dieter Schuh for their collaboration, especially for fulfilling my wishes for some really unusual superlattice structures.
- Dr. Dimitry Paveliev for his cooperation on superlattice frequency multipliers.
- Our technicians Klaus Lachner, Rudi Reisser and Toni Humbs for their support in all technical questions. Special thanks to Klaus Lachner for keeping the unmanageable RIE running.
- The staff of the mechanical workshop who managed to fabricate unbelievably tiny structures, especially Walter Wendt, who carried precision mechanics to the extremes.
- The members of the electronics workshop for their advice and support and lots of coffee breaks.
- The Graduiertenkolleg 638 for the financial support during the last three years and for providing me with the opportunity to expand my physical horizons.

- The final correctors of this work, Florian, Dominik, Dana, Andreas.
- All my friends at the physics department for all the enjoyable time together.
- My family for love and support.

9 Appendix: Comparison to a superlattice quintupler

A quintupler, which converts pump radiation to fifth harmonic radiation appears to be a promising way to realize a radiation source for the terahertz frequency range. In this chapter, a GaAs/AlAs superlattice quintupler is presented. A comparison of these results to the SPO and a theoretical analysis demonstrate the difference in the operating mechanism of the quintupler and the SPO mechanism.

Quintupler design

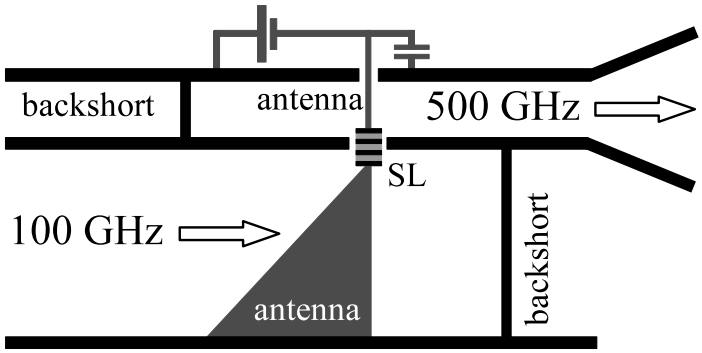

Figure 9.1: Schematic of a superlattice quintupler. The fifth harmonic waveguide has a frequency cut-off near 450 GHz which prevents the production of third harmonic radiation.

The design of the quintupler (fig. 9.1) was quite similar to that of the SPO (see fig. 4.1): it consisted of two waveguides, one for pump radiation (75 GHz to 110 GHz) and one for fifth harmonic radiation. In contrast to the SPO design, the resonator had a cut-off frequency of 450 GHz, which suppressed harmonics lower than the fifth. Both waveguides were terminated by fix backshorts. A quasiplanar superlattice device was coupled to the pump waveguide by a finline antenna and to the fifth harmonic waveguide by a thin wire antenna. The superlattice device was designed similarly to

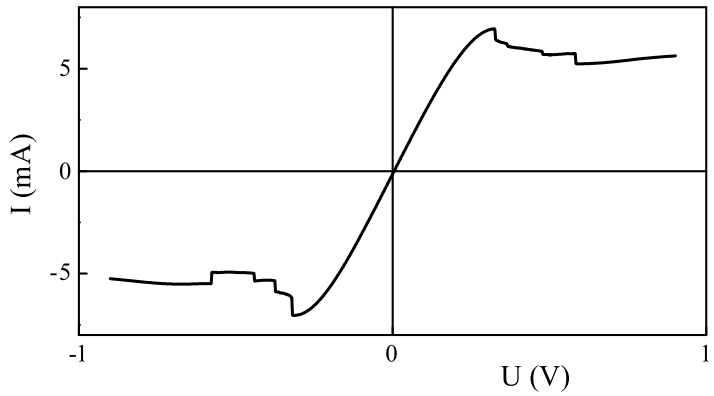

Figure 9.2: Current-voltage characteristic of the superlattice device used in the quintupler.

the one used in the SPO (fig. 4.3).

Experimental results

The quintupler design allowed to measure the I-V curve of the superlattice device. The quintupler was pumped with a Gunn oscillator (frequency $\sim$ 100 GHz) while the pump power was continuously variable by an attenuation element. The spectrum of the radiation was analyzed with a Fabry-Perot interferometer, and a Golay cell detector.

Current-voltage characteristic

The current-voltage characteristic (fig. 9.2) showed an ohmic region at small voltage, a peak (I_p = 7 mA) at a critical voltage (U_c = 0.3 V) and a region of negative differential mobility at higher voltage. Jumps in the current voltage characteristic at voltages exceeding U_c indicated the formation of space charge domains, accompanied by an inhomogeneous electric field distribution. Radiation from the quintupler was coupled out through a horn antenna.

Spectrum

The Fabry-Perot interferogram (fig. 9.3) revealed that emission consisted mainly of fifth harmonic radiation (peak distance 0.3 mm= $\lambda_5/2$, where λ_5 is the wavelength of fifth harmonic radiation). Peaks from sixth and seventh harmonic radiation were also visible, but were by a factor of about ten weaker. The occurrence of sixth harmonic radiation can be explained by an asymmetry of the superlattice leading to a non perfect

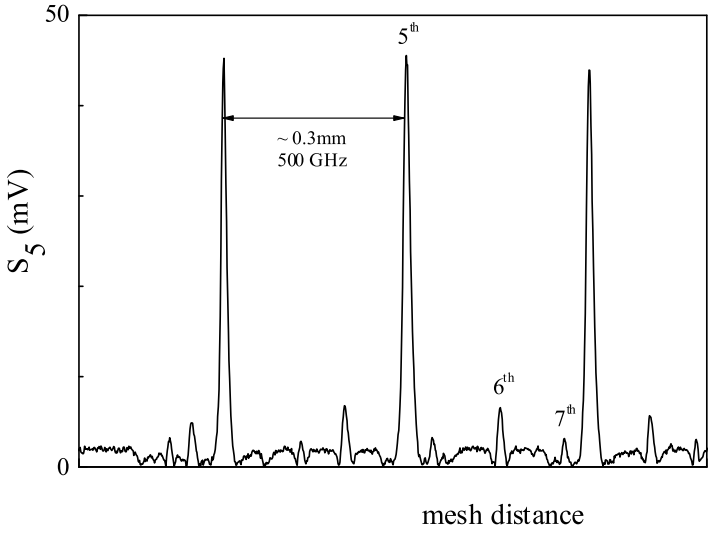

Figure 9.3: Fabry-Perot interferogram obtained with a quintupler pumped at a frequency of 100 GHz.

antisymmetry of the I-V curve.

Starting behavior

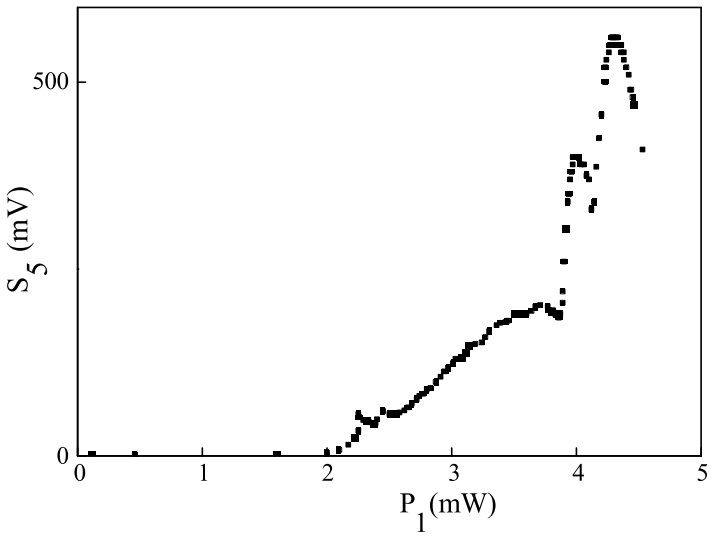

Figure 9.4: Fifth harmonic signal for different pump powers.

The fifth harmonic signal S_5 showed a steep increase (fig. 9.4) if a pump power of ~ 2 mW was exceeded. After a moderate rise (inbetween 2.3 mW and 3.9 mW), the signal increased very strongly again, by a factor of three (between 3.9 mW and 4.3 mW). However, there were no jumps in the signal or other signs for threshold behavior. The

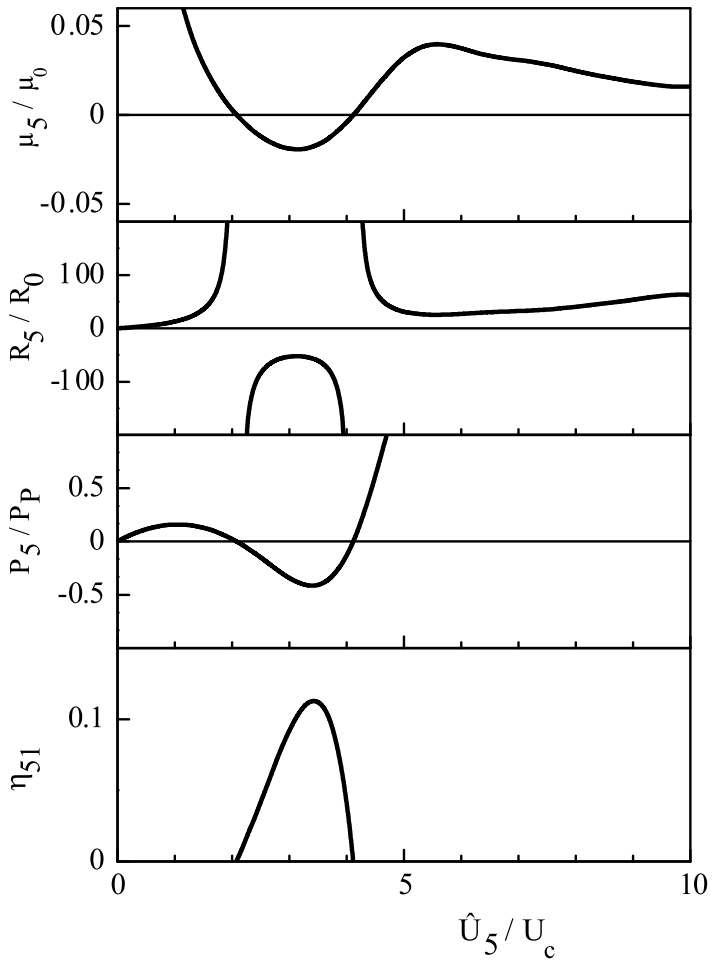

Figure 9.5: Mobility, resistance, power and conversion efficiency for the fifth harmonic in a quintupler for different fifth harmonic amplitudes at a pump frequency of 100 GHz. The mobility is positive for zero fifth harmonic amplitude which prevents the onset of parametric oscillation at the fifth harmonic.

signal always varied continuously. An effect of feedback could not be demonstrated. The output power of the quintupler ($\sim 10\,\mu$W) was measured with a thermal power meter. The corresponding efficiency was of the order of 0.1 percent.

Theoretical results

Calculations for a superlattice (fig. 9.5) in a pump field ($\hat{U}_1 = 5\,U_c,\ \nu_1 = 100$ GHz) and a fifth harmonic field ($\hat{U}_5,\ \nu_5 = 500$ GHz) show that in a superlattice, for small fifth harmonic amplitudes, the fifth harmonic mobility μ_5 is positive, as well as the resistance R_5 and the power P_5. At small amplitudes $\hat{U}_5$ of the fifth harmonic, radiation is absorbed by the superlattice. Gain is only obtained if $\hat{U}_5$ exceeds a critical value.

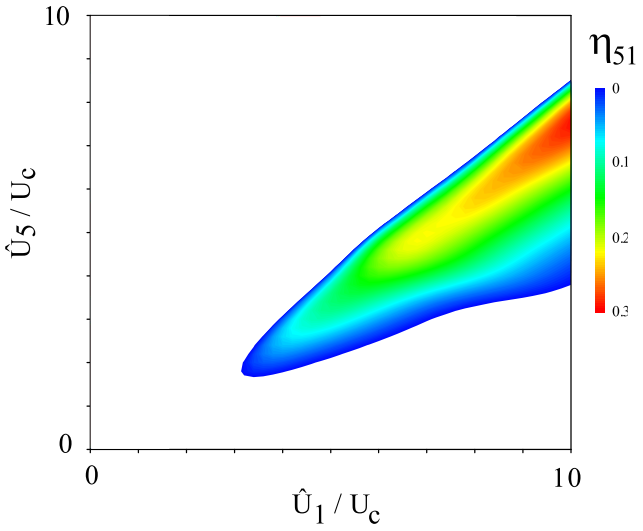

Figure 9.6: Conversion efficiency η_{51} of a quintupler for different pump and fifth harmonic amplitudes.

Then, the superlattice amplifies fifth harmonic radiation, which can lead to oscillations. The results show that in a quintupler, oscillation cannot start from a small signal or from noise. A contour diagram (fig. 9.6) reveals that, in order to obtain oscillation at 500 GHz, a threshold pump power of at least $3.5\,U_c$ is necessary together with a fifth harmonic voltage amplitude $\hat{U}_5 \gtrsim 2\,U_c$. At higher pump power and fifth harmonic amplitude, the conversion efficiency η_{51} can exceed 20 percent.

Discussion

In contrast to the SPO, in a quintupler, generation of the fifth harmonic is not due to parametric gain but due to frequency multiplication according to the nonlinear current-voltage curve of the superlattice or due to the periodic creation and annihilation of space charge domains. The smooth starting behavior of the quintupler without a threshold-like onset indicates that parametric oscillations do not occur, which is in agreement with the theoretical results.

Bibliography

[1] P. H. Siegel, "Terahertz technology", *Microwave Theory and Techniques, IEEE Transactions on*, vol. 50, no. 3, pp. 910–928, 2002.

[2] T. G. Phillips and J. Keene, "Submillimeter astronomy", *Proc. IEEE*, vol. 80, no. 11, pp. 1662–1678, 1992.

[3] Th. de Graauw and F. P. Helmich, "Herschel-HIFI: the heterodyne instrument for the far infrared", in *The promise of the Herschel space observatory*, G. L. Pilbratt, J. Cernicharo, A. M. Heras, T. Prusti, and R. Harris, Eds., Toledo, 2001.

[4] C. P. Endres, F. Lewen, T. F. Giesen, S. Schlemmer, D. G. Paveliev, Y. I. Koschurinov, V. M. Ustinov, and A. E. Zhucov, "Application of superlattice multipliers for high-resolution terahertz spectroscopy", *Review of Scientific Instruments*, vol. 78, no. 4, pp. 043106, 2007.

[5] F. F. Federici, B. Schlkin, F. Huang, G. D. Dale, R. Barat, F. Oliveira, and D. Zimdars, "Terahertz imaging and sensing for security applications - explosives, weapons, drugs", *Semiconductor Science and Technology*, vol. 20, pp. 266–280, 2005.

[6] R. Ammicht Quinn and A. Pabst, "Ethical advisory service for terasec: Report", Interfakultäres Zentrum für Ethik in der Wissenschaft, Universität Tübingen, 2007.

[7] A. Gatesman, A. J. andDanylov, T. M. Goyette, J. C. Dickinson, R. H. Giles, W. Goodhue, J. Waldman, W. E. Nixon, and W. Hoen, "Terahertz behavior of optical components and common materials", in *Proceedings of the SPIE Vol 6212: Terahertz for Military and Security Applications IV*, Mark J. Rosker James O. Jensen Dwight L. Woolard, R. Jennifer Hwu, Ed., 2006.

[8] B. S. Williams, "Terahertz quantum cascade lasers", *Nature Photonics*, vol. 1, pp. 517–525, 2007.

[9] M. A. Belkin, F. Capasso, A. Belyanin, D. L. Sivco, A. Y. Cho, D. C. Oakley, C. J. Vineis, and G. W. Turner, "Terahertz quantum-cascade-laser source based on intracavity difference-frequency generation", *Nature Photonics*, vol. 1, pp. 288 – 292, 2007.

[10] K. Kawase, M. Sato, T. Taniuchi, and H. Ito, "Coherent tunable THz-wave generation from LiNbO3 with monolithic grating coupler", *Applied Physics Letters*, vol. 68, no. 18, pp. 2483–2485, 1996.

[11] T. Edwards, D. Walsh, M. Spurr, C. Rae, M. Dunn, and P. Browne, "Compact source of continuously and widely-tunable terahertz radiation.", *Opt. Express*, vol. 14, no. 4, pp. 1582–1589, 2006.

[12] E. R. Brown, K. A. McIntosh, K. B. Nichols, and C. L. Dennis, "Photomixing up to 3.8 THz in low-temperature-grown GaAs", *Applied Physics Letters*, vol. 66, no. 3, pp. 285–287, 1995.

[13] H. Eisele, "Active two-terminal devices as sources at THz frequencies: concepts, performance, and trends", 2006, vol. 6257, p. 62570, SPIE.

[14] L. Esaki and R. Tsu, "Superlattice and negative differential conductivity in semiconductors", *IBM Journal of research and developement*, vol. 14, no. 1, pp. 61–65, 1970.

[15] A. Sibille, J. F. Palmier, H. Wang, and F. Mollot, "Observation of Esaki-Tsu negative differential velocity in GaAs/AlAs superlattices", *Physical Review Letters*, vol. 64, no. 1, pp. 52–55, 1990.

[16] J. Feldmann, K. Leo, J. Shah, D. A. B. Miller, J. E. Cunningham, T. Meier, G. von Plessen, A. Schulze, P. Thomas, and S. Schmitt-Rink, "Optical investigation of Bloch oscillations in a semiconductor superlattice", *Phys. Rev. B*, vol. 46, no. 11, pp. 7252–7255, 1992.

[17] Christian Waschke, Hartmut G. Roskos, Ralf Schwedler, Karl Leo, Heinrich Kurz, and Klaus Köhler, "Coherent submillimeter-wave emission from Bloch oscillations in a semiconductor superlattice", *Physical Review Letters*, vol. 70, no. 21, pp. 3319–3322, 1993.

[18] S.A. Ktitorov, G.S. Simin, and V.Ya. Sindalovskii, "Bragg reflections and the high-frequency conductivity of an electronic solid-state plasma", *Sov. Phys. Solid State*, vol. 13, no. 8, pp. 1872–1874, 1971.

[19] H. Kroemer, "Large-amplitude oscillation dynamics and domain suppression in a superlattice Bloch oscillator", arXiv: cond-mat/0009311v1, 2000.

[20] P. G. Savvidis, B. Kolasa, G. Lee, and S. J. Allen, "Resonant Crossover of Terahertz Loss to the Gain of a Bloch Oscillating InAs/AlSb Superlattice", *Physical Review Letters*, vol. 92, no. 19, pp. 196802 1–4, 2004.

[21] E. Schomburg, N. V. Demarina, and K. F. Renk, "Amplification of a terahertz field in a semiconductor superlattice via phase-locked k-space bunches of Bloch oscillating electrons", *Physical Review B*, vol. 67, no. 15, pp. 155302, 2003.

[22] M. Büttiker and H. Thomas, "Current instability and domain propagation due to Bragg scattering", *Physical Review Letters*, vol. 38, no. 2, pp. 78–80, 1977.

[23] E. Schomburg, R. Scheuerer, S. Brandl, K.F. Renk, D.G. Pavel'ev, Yu. Koschurinov, V. Ustinov, A. Zhukov, A. Kovsh, and P.S. Kop'ev, "InGaAs/InAlAs superlattice oscillator at 147 GHz", *Electronics Letters*, vol. 35, no. 17, pp. 1491–1492, 1999.

[24] A. Meier, A. Glukhovskoy, M. Jain, B. I. Stahl, K. F. Renk, P. Tranitz, and W. Wegscheider, "Semiconductor-superlattice higher harmonic oscillator for generation of millimeter waves", in *29. International Conference on Infrared and Millimeter Waves*, Karlsruhe, 2004.

[25] T. Feil, H.-P. Tranitz, M. Reinwald, and W. Wegscheider, "Electric-field stabilization in a high-density surface superlattice", *Applied Physics Letters*, vol. 87, no. 21, pp. 212112, 2005.

[26] F. Klappenberger, K. F. Renk, P. Renk, B. Rieder, Yu. I. Koshurinov, D. G. Pavelev, V. Ustinov, A. Zhukov, M. Maleev, and A. Vasilyev, "Semiconductor-superlattice frequency multiplier for generation of submillimeter waves", *Applied Physics Letters*, vol. 84, pp. 3924, 2004.

[27] Yu. A. Romanov, "Upwards parametric frequency conversion in superlattices", *Radiophys. Quantum Electron.*, vol. 23, no. 5, pp. 421–428, 1980, translated from: Izvestiya Vysshikh Uchebnykh Zavedenii, Radiofizika, Vol. 23, No. 5, pp. 617 625, 1980.

[28] V. V. Pavlovich, "Nonlinear amplification of electromagnetic waves in a semiconductor with a superlattice", *Sov. Phys. Solid State*, vol. 19, no. 1, pp. 54–56, 1977, translated from: Fizika Tverdogo Tela,vol.19, no.1, pp. 97-99, 1977.

[29] F. Klappenberger and K.F. Renk, "Proposal of a microwave-driven semiconductor superlattice oscillator for generation of THz radiation", *International Journal of Infrared and Millimeter Waves*, vol. 25, no. 3, pp. 429–438, 2004.

[30] G. Bastard, *Wave mechanics applied to semiconductor heterostructures*, Halsted Press, New York, 1988.

[31] A. A. Ignatov, E. Schomburg, J. Grenzer, K. F. Renk, and E. P. Dodin, "THz-field induced nonlinear transport and dc voltage generation in a semiconductor superlattice due to Bloch oscillations", *Z. Phys. B*, vol. 98, no. 2, pp. 187–195, 1995.

[32] K. F. Renk, B. I. Stahl, A. Rogl, T. Janzen, D. G. Pavel'ev, Yu. I. Koshurinov, V. Ustinov, and A. Zhukov, "Subterahertz superlattice parametric oscillator", *Physical Review Letters*, vol. 95, no. 12, pp. 126801 1–4, 2005.

[33] K. F. Renk and L. Genzel, "Interference filters and Fabry-Pérot interferometers for the far infrared", *Applied Optics*, vol. 1, no. 5, pp. 643–648, 1962.

[34] K. F. Renk, A. Rogl, B. Stahl, A. Meier, Yu. I. Koschurinov, D. G. Pavelev, V. Ustinov, A. Zhukov, N. Maleev, and A. Vasilyev, "Semiconductor-superlattice frequency mixer for detection of submillimeter waves", *Int. J. Infrared Millim. Waves*, vol. 27, pp. 373–380, 2006.

[35] M. Häussler, R. Scheuerer, K. F. Renk, Yu. Koschurinov, and D. G. Pavel'ev, "Microwave frequency multiplication by use of space charge domains", *Electronics Letters*, vol. 39, no. 7, pp. 628–629, 2003.

[36] R. Scheuerer, D. G. Pavelev, K. F. Renk, and E. Schomburg, "Frequency multiplication using induced dipole domains in a semiconductor superlattice", *Physica E*, vol. 22, pp. 797–803, 2003.

[37] K. N. Alekseev, M. V. Gorkunov, N. V. Demarina, T. Hyart, N. V. Alekseeva, and A. V. Shorokhov, "Suppressed absolute negative conductance and generation of high-frequency radiation in semiconductor superlattices", *Europhysics Letters*, vol. 73, no. 6, pp. 934–940, 2006.

[38] B. I. Stahl, A. Rogl, and K. F. Renk, "A theoretical study of operation conditions for a terahertz superlattice parametric oscillator", *Physics Letters A*, vol. 359, no. 5, pp. 512–515, December 2006.

[39] A. Rogl, K. F. Renk, B. I. Stahl, C. Reichl, D. Schuh, and W. Wegscheider, "Double-resonance semiconductor superlattice parametric oscillator for generation of subterahertz radiation", *accepted by Int. J. Infrared Millim. Waves*, June 2008.